

Research Paper

Rainwater accumulation model related to tectono-stratigraphic assessment for bradyseism at Campi Flegrei, Italy

Nicola Scafetta, Annamaria Lima, Alfonsa Milia, Frank Spera, Robert J. Bodnar, Benedetto De Vivo, Linda Daniele

PII: S1674-9871(26)00010-1

DOI: <https://doi.org/10.1016/j.gsf.2026.102256>

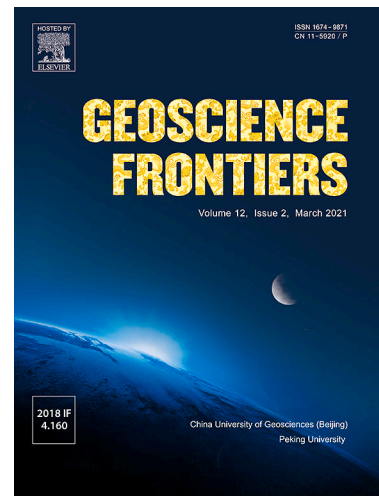
Reference: GSF 102256

To appear in: *Geoscience Frontiers*

Received Date: 15 September 2025

Revised Date: 24 December 2025

Accepted Date: 13 January 2026



Please cite this article as: N. Scafetta, A. Lima, A. Milia, F. Spera, R.J. Bodnar, B.D. Vivo, L. Daniele, Rainwater accumulation model related to tectono-stratigraphic assessment for bradyseism at Campi Flegrei, Italy, *Geoscience Frontiers* (2026), doi: <https://doi.org/10.1016/j.gsf.2026.102256>

This is a PDF of an article that has undergone enhancements after acceptance, such as the addition of a cover page and metadata, and formatting for readability. This version will undergo additional copyediting, typesetting and review before it is published in its final form. As such, this version is no longer the Accepted Manuscript, but it is not yet the definitive Version of Record; we are providing this early version to give early visibility of the article. Please note that Elsevier's sharing policy for the Published Journal Article applies to this version, see: <https://www.elsevier.com/about/policies-and-standards/sharing#4-published-journal-article>. Please also note that, during the production process, errors may be discovered which could affect the content, and all legal disclaimers that apply to the journal pertain.

1 **Research Paper**

2

3 **Rainwater accumulation model related to tectono-stratigraphic assessment for**
4 **bradyseism at Campi Flegrei, Italy**

5

6

7 Nicola Scafetta^{a,*}, Annamaria Lima^a, Alfonsa Milia^b, Frank Spera^c, Robert J. Bodnar^d, Benedetto De Vivo^{a,d,e,f},
8 Linda Daniele^g

9

10 ^a Dipartimento di Scienze della Terra, dell'Ambiente e delle Risorse (DiSTAR), University of Naples Federico
11 II, Complesso Universitario di Monte Sant'Angelo, Via Cintia 26, 80126 Naples, Italy.12 ^b Istituto Ambiente Marino Costiero, CNR, Calata Porta di Massa, Porto di Napoli 80133, Italy.13 ^c Department of Earth Science and Earth Research Institute, University of California, Santa Barbara, CA
14 93106, USA.15 ^d Department of Geosciences, Virginia Tech, 4044 Derring Hall, Blacksburg, Virginia 24061, USA.16 ^e Nanjing University, Nanjing 210023, China.17 ^f Hubei Polytechnic Univ., Huangshi, China.18 ^g Department of Geology, FCFM, University of Chile, Santiago, Chile.

19

20 * Correspondent: nicola.scafetta@unina.it

21

22 **Abstract**

23

24 The Campi Flegrei (CF) volcanic system near Naples, Italy, poses a significant hazard due to
25 bradyseism — a slow vertical ground deformation resulting in either uplift or subsidence. Indeed,
26 between January 2005 and January 2025, the urban area of Pozzuoli experienced approximately 1.4
27 m of uplift (GNSS RITE Station). The bradyseism is driven by a combination of hydrothermal and
28 magmatic processes, whereby pressurized magmatic fluids generated by deep magma crystallization
29 accumulate beneath an impermeable layer that regulates fluid exchange between upper hydrostatic
30 and lower lithostatic systems. This study introduces a new perspective through a detailed
31 reconstruction of the stratigraphic-tectonic architecture of the CF area that enables identification of
32 structural controls on seismicity, deformation, and fluid migration, and the role of meteoric water.
33 Seismicity beneath the Pozzuoli-Solfatara area occurs at shallower depths near the top of an anticline,
34 whereas deeper earthquakes in Pozzuoli Bay occur in synclinal environments. The anticline beneath

35 Pozzuoli facilitates hydrothermal fluid pressurization in two main reservoirs beneath two relatively
36 impermeable units. The shallow reservoir, referred to as Unit C, is located at a depth of approximately
37 1.0 to 2.0 km and acts as a reservoir for meteoric water infiltration. The deeper reservoir, referred to
38 as Unit A, occurs at a depth of about 2.0 and 4.0–4.5 km, where magmatic fluids generated by second
39 boiling in the underlying magma accumulate. An impermeable unit of marine sediments, referred to
40 as Unit B, is located at ~2 km depth and separates Units A and C. The shallow reservoir is bounded
41 at the top by a relatively impermeable unit mainly made up of pyroclastic deposits. We developed a
42 simplified hydrogeological model using rainfall data dating back to 1950 to assess the role of meteoric
43 water in bradyseism at CF. We found a strong correlation between subsurface water infiltration and
44 vertical ground deformation observed at the Pozzuoli RITE Station, which corresponds to the crest
45 of the anticline. Our results suggest that meteoric water contributes to interannual uplift fluctuations
46 of up to ~5 cm and accounts for over 20% of the total uplift recorded between 2005 and 2025.
47 Furthermore, a shortening of recharge time-lag — from about four years to three years since 2010 —
48 indicates enhanced fracturing and infiltration rates. These findings highlight the previously
49 underestimated role of meteoric water in driving deformation and seismicity at CF. Our results also
50 suggest that geoengineering involving targeted surface drainage interventions could mitigate ongoing
51 ground instability and seismic hazards in the region.

52

Keywords: Pozzuoli-Solfatara bradyseism; Anticline stratigraphic structure; Hydrological model; Meteoric water infiltration; Pyroclastics.

1. Introduction

57 The Campanian active volcanic region, encompassing the Campi Flegrei (CF) and the Somma-
 58 Vesuvius complexes in the province of Naples (Italy), represents an area of considerable risk, as over
 59 three million people are exposed to significant volcanic and seismic hazards (De Vivo and Rolandi,
 60 2020; Carlino, 2021). Currently, CF is a major focus of concern due to accelerating ground uplift
 61 since 2005. CF is under constant monitoring and extensive study and has been the subject of
 62 numerous scientific investigations addressing its geochemical, geodetic, geological, seismological,
 63 and structural characteristics. While there is no consensus regarding the causes of this phenomenon,
 64 it is widely recognized that fluids within the geothermal system - of magmatic, marine, and/or
 65 meteoric origin - play a critical role (e.g., Caprarelli et al., 1997; Bodnar et al., 2007; Caliro et al.,
 66 2025).

67 Within CF, the Pozzuoli-Solfatara area has experienced the maximum uplift and most intense
 68 seismic activity. This shallow seismicity could have a hydrological influence associated with a
 69 decrease in the effective stress due to an increase in pore pressure that accompanies groundwater
 70 recharge (Casertano et al., 1976; Bonafede and Mazzanti, 1997; Wang and Manga, 2021). Shallow
 71 earthquake swarms at CF often exhibit relatively high *b* values in the Gutenberg-Richter scaling
 72 relation $\log_{10} N = a - bM$, where *N* is the cumulative number of earthquakes greater than magnitude
 73 *M*, and *a* and *b* are constants (Tramelli et al., 2024). High *b* values have been associated with pore
 74 pressure, thermal gradients and matrix heterogeneity (Warren and Latham, 1970; Wyss, 1973;
 75 Wiemer and McNutt, 1997). All of these factors may be significant at CF. Several studies have
 76 attributed seasonal variations of seismicity in other volcanic areas to groundwater recharge (e.g., Saar
 77 and Manga, 2003; Montgomery-Brown et al., 2019) via poroelastic effects. A correlation between
 78 precipitation and earthquakes (e.g., Roth et al., 1992; Jimenez and Garcia-Fernandez, 2000; Hainzl
 79 et al., 2006; Kraft et al., 2006; Husen et al., 2007) supports the idea that pore pressure changes caused
 80 by recharge processes can influence seismicity. For example, at the edge of Long Valley caldera, in
 81 California, large seasonal variations in precipitation occur, and seismicity rate is ~37 times greater
 82 during spring snowmelt than during the driest period of the year (Montgomery-Brown et al., 2019).
 83 At regional scales, changes in hydrological loading rate and induced pore pressure changes may
 84 contribute to seasonal variations in seismicity (Ueda and Kato, 2019). Underground water
 85 accumulation increases pore pressure, and can reduce the stability of existing faults, leading to both
 86 ground uplift and earthquakes mostly in geothermal regions where heated fluids expand, amplifying
 87 pressure, and contribute to ground uplift (Todesco, 2021). These phenomena are governed by the
 88 interplay of hydrogeological, mechanical, and geophysical factors (Wang and Manga, 2021).

89 Relative to the surrounding regions, CF experiences higher precipitation rates, which also leads
 90 to some exceptional flash floods (Fortelli et al., 2019). Morphologically, the CF region is
 91 characterized by numerous volcanic vents, such as the Astroni, upstream of the Solfatara area, that,
 92 as first hypothesized by Scafetta and Mazzarella (2021), could act as a funnel collecting large
 93 volumes of rainwater that can readily infiltrate the subsurface of the CF hydrothermal system through
 94 extensive fracturing in the upper 3 km (Cipriani et al., 2008), likely contributing to the surface uplift.

95 Although rainfall, atmospheric pressure variations and tidal oceanic loading have been posited as
 96 factors influencing seismic and volcanic activity (Mazzarella and Palumbo, 1989; Mastin, 1993;
 97 Farquharson and Amelung, 2020), these aspects have received relatively little attention at CF.
 98 Nevertheless, some studies have linked rainfall and tidal patterns to local seismicity recorded during
 99 the moderate uplift phases of bradyseism unrest between 2008 and 2020 (Petrosino et al., 2018;
 100 Scafetta and Mazzarella, 2021). Earlier epochs of uplift and increased concurrent seismic activity in
 101 1970 and 1982 were preceded by anomalously large increases in oceanic loading and rainfall,
 102 although Palumbo (1985) could not clearly separate the rainfall and oceanic loading effects. The

103 observation that periods of active uplift correlate with small changes in stress due to solar-lunar tidal
 104 effects (oceanic loading) and rainfall going back over a half-century indicates that the state of stress
 105 at depth is sensitive to relatively weak external forces and does not require the addition of new
 106 magma. However, the thermal engine that ultimately drives the CF hydrothermal-magmatic
 107 supersystem should not be neglected. Indeed, since the pioneering work by De Vivo and Lima (2006)
 108 up to the most recent study by Lima et al. (2025a, and reference therein), it was shown that the
 109 ultimate heat engine that drives bradyseism at CF must be the deep magmatic system at >7.5 km
 110 depth. The extent of fracturing does not represent competition between fluid escape and injection
 111 rates because the release of magmatic fluid and upward transport of magmatic heat is continuous over
 112 time. Instead, the differential expansion of rock and pore fluid due to heating gives rise to poroelastic
 113 effects (Detournay and Cheng, 1993) including fluid migration and fracture propagation. Without the
 114 thermal effects of the magmatic engine these effects would not occur.

115 The aim of this study is to assess whether and how rainwater infiltration on interannual to
 116 multidecadal timescales contributes to bradyseism in the CF. To achieve this goal, we developed a
 117 schematic-conceptual model to simulate groundwater recharge as a function of the local precipitation
 118 record and its hypothesized discharge to the sea. For this reason, it was also necessary to reconstruct
 119 the CF stratigraphic and structural architecture to highlight the impermeable and permeable units
 120 along with their distribution within the CF system. More specifically, first we constructed a schematic
 121 hydrological model related to the complex stratigraphy underlying the CF area and identified the
 122 recharge areas in CF in relationship to areas experiencing seismic activity and bradyseism. Then, we
 123 adopted a realistic - albeit simplified - hydrogeological model to dynamically evaluate the recharge
 124 level of the reservoir beneath Pozzuoli and its temporal variation in response to the local rainfall
 125 record since 1950. An inverse approach, required by the hydrological model, is adopted to determine
 126 the hydraulic conductivity of the reconstructed strata in the CF area. Developing a physics-based
 127 reductionist approach in which all known physical processes are considered to compute the output is
 128 impractical due to the excessive number of unknowns.

129

130 2. Overview and history of bradyseism in the Campi Flegrei volcanic system

131

132 2.1. Geologic framework of the CF area

133

134 The CF volcanic system is located along the coast of the Campanian Plain, on the eastern margin of
 135 the Tyrrhenian Sea where the most recent back-arc extensional basins developed (Fig. 1a).

136 Some authors have attempted to reconstruct the CF stratigraphic pattern through seismic
 137 tomography and magnetotelluric data interpretation (e.g., De Landro et al., 2025; Isaia et al., 2025);
 138 however, in our view, such data remain insufficient to provide a detailed understanding of the area's
 139 stratigraphic and tectonic architecture. Reconstruction of the stratigraphic architecture and the
 140 structural framework is a fundamental first step to constrain the lateral and vertical extents of
 141 impermeable strata, and the permeability characteristics of the various stratigraphic units. To achieve
 142 this goal, because CF stratigraphy is the result of the interplay between tectonics, sediment supply
 143 and volcanic activity, we consider the evolution of the Campanian Margin (Fig. 1b) starting from the
 144 Lower Pleistocene when the first clastic sediments covered the Meso-Cenozoic substrate. In
 145 particular, three first-order tectonic events took place during this period (Milia and Torrente, 2020).

146 The earliest tectonic event is represented by the eastward opening of the Vavilov back-arc basin
 147 (Fig. 1a). The initial event led to the formation of the Lower Pleistocene NW-trending normal faults,
 148 which affected the exposed Apennine chain, and created symmetrical basins (e.g., the Sorrento
 149 graben; Milia and Torrente, 1997). Unit A (Fig. 1c), consisting of a sedimentary succession ranging
 150 from continental to shallow marine environments, was deposited during this stage (Milia and
 151 Torrente, 1999, 2015a, 2015b; Milia et al., 2003). These deposits, dated to 1 Ma, have been
 152 documented in the Trecase and Cancello boreholes, located northwest and southeast of the CF,
 153 respectively, and in outcrops along the margin of the Campanian Plain (Bernasconi et al., 1981;
 154 Brocchini et al., 2001; Milia and Torrente, 2015; Cerrone et al., 2021).

155 The second tectonic event corresponds to the extension toward the southeast of the Campanian
 156 Margin. This event led to the formation of Middle Pleistocene NE-trending normal faults, generating
 157 asymmetric grabens — most notably the Naples Bay–CF half graben (Fig. 1c). During this stage,
 158 Unit B (0.7 – 0.4 Ma) was deposited. This period marked both the uplift of the Sorrento Peninsula
 159 and the rapid subsidence of the CF basin, corresponding to the deposition of a relatively thin strata
 160 of deep-water environment sediments (Milia and Torrente, 1999). These deposits (Unit B, Fig. 1c)
 161 consist of clay-rich lithologies forming a transgressive unit that blankets the basin and were identified
 162 in the Trecase, Mofete, and S. Vito boreholes (Rosi and Sbrana, 1987; Brocchini et al., 2001; Marini
 163 et al., 2025). Subsequently, the half graben was infilled by a thick regressive unit — Unit C (Milia,
 164 and Torrente, 1999) — made up of three substantial lowstand prograding wedges. Unit C (Fig. 1c),
 165 dated between approximately 0.4 Ma and 0.1 Ma, consists of silt, sand, and conglomerate. During
 166 this phase, numerous volcanic products, primarily composed of lava, were interlayered within the
 167 stratigraphic succession. These have been documented in the Trecase borehole (Brocchini et al.,
 168 2001), in the southern Gaeta Bay offshore region and in the Mofete boreholes (Rosi and Sbrana,
 169 1987), and in the Penta Palummo (PP) area shown in Fig. 1b (Milia et al., 2006).

170 The third tectonic event relates to a change in the direction of extension along the margin towards
 171 the east-southeast (Fig. 1a, 1b). This event, which shaped the current structural configuration,
 172 occurred over the past 0.1 Ma and is associated with major ignimbrite eruptions along the Campanian
 173 Margin (De Vivo et al., 2001; Rolandi et al., 2003). For the first time, the continental shelf of Naples
 174 Bay and the Campanian Plain recorded simultaneous activity of normal faulting and ignimbrite
 175 volcanism (Milia, 2000; De Vivo et al., 2001; Torrente et al., 2010). As a result of this tectonic event,
 176 pre-existing NW–NE trending normal faults were reactivated, and thick ignimbrite wedges
 177 accumulated along the Campanian Margin – Unit D in Fig. 1c (Milia and Torrente, 2011, 2020). In
 178 the last 14 ka (post-Neapolitan Yellow Tuff), an intricate fault system developed, producing localized
 179 transpressional tectonics. This tectonic style led to a local compression within the CF area and the
 180 formation of a detachment fold, whose anticline culminates beneath the city of Pozzuoli (Fig. 2a;
 181 Milia and Torrente, 2000). The folding extends from the Epitaffio Valley, west of Pozzuoli, to the
 182 Bagnoli area (Milia et al., 2000; Milia and Giordano, 2002). Fig. 2c illustrates the eastern flank of the
 183 syncline and Fig. 2d shows the faulted and folded strata offshore the city of Pozzuoli. The Solfatara
 184 volcano (ca. 4 ka) (Fig. 2b), located on the crest of the anticline, is a maar/diatreme structure that
 185 formed through phreato-magmatic processes, with faults extending to depths of approximately 2–3
 186 km (Cipriani et al., 2008; Marini et al., 2022). Its structural configuration can be interpreted as being
 187 linked to opening fractures/faults commonly associated with crestal anticline settings associated with
 188 a tangential-longitudinal strain mechanism (Ramsey, 1967).

189

190 2.2. *Bradyseismic activity at Campi Flegrei*

191

192 The penultimate period of significant volcanic activity in CF occurred between about 5500 and 3500
 193 years ago, during which numerous eruptions took place with the formation of several eruptive centers
 194 including on the eastern side of CF at Agnano-Monte Spina, Astroni and Solfatara (Fig. 2b) (Orsi et
 195 al., 2009). In 1538 the Monte Nuovo eruption occurred; this is the only historic eruption known to
 196 have been preceded by significant ground uplift. In the years preceding the Monte Nuovo eruption
 197 about 7 m asl of ground uplift was reported (Rolandi et al., 2025) in a small area including the vent.
 198 Following the 1538 eruption, a subsidence phase began and persisted until 1950, at which point an
 199 uplift phase occurred from 1950 to 1952 (Rolandi et al., 2025). Subsequent uplift episodes were
 200 recorded from 1969 to 1972 and 1982 to 1984. The 1982–1984 bradyseism event, the most
 201 extensively studied, resulted in an uplift of 186 cm that was accompanied by low-magnitude seismic
 202 swarms (maximum $M = 4.0$), with up to 610 seismic events occurring within a few hours (Del Gaudio
 203 et al., 2010). After 1984, a period of subsidence ensued, lasting approximately 20 years at an average
 204 rate of ~4 cm/year, culminating in a total subsidence of ~93 cm. During this subsidence phase, short
 205 episodes of mini uplift, lasting a few months, were observed in 1989, 1994, 2000, and again during
 206 2012–2013, coinciding with the slow uplift phase that began in 2005 (Fig. 3) (Orsi, 2022). This
 207 accelerating uplift phase, ongoing to the present day, is a source of concern due to intensified seismic
 208 activity, including a $M = 4.6$ event that occurred on March 13, 2025, at a depth of 2.5 km below the
 209 seafloor in front of “Località la Pietra” in Bagnoli and east of Solfatara along the main fault (Figs. 2
 210 and 4). The *Osservatorio Vesuviano - Istituto Nazionale di Geofisica e Vulcanologia* (OV-INGV)
 211 reported that the waveform for the latter event consists of two earthquake signals whose first arrivals
 212 occur in very rapid sequence (OV-INGV Surveillance Bulletins, March 2025). In addition, increasing
 213 fluid emission and fumarolic tremor amplitude, which is indicative of hydrothermal activity, were
 214 registered along with uplift of about 1.5 m from January 2005 to September 2025 in the Pozzuoli area
 215 (cf. Chiodini et al., 2017).

216

217 2.3. *A model to explain CF bradyseism*

218

219 The hydrothermal model to describe bradyseism and ground deformation at CF is based on research
 220 by the current authors over the past several decades and summarized by De Vivo and Lima (2006),
 221 Bodnar et al. (2007), De Vivo et al. (2009), Cannatelli et al. (2020), and Lima et al. (2009, 2021,
 222 2025a). Our model proposes that the fundamental driver of bradyseism at CF is the magmatic system
 223 located at depths greater than 7.5 km (Fig. 4). During crystallization, the magma becomes volatile
 224 (H_2O , CO_2) saturated and releases magmatic fluid that accumulates beneath an impermeable cap that
 225 occasionally fractures, allowing the magmatic fluids to migrate upwards. Upward migrating
 226 magmatic fluids accumulate in Unit A beneath the impermeable Unit B (Fig. 4), which episodically
 227 fractures in response to the increased fluid pressure and allows magmatic fluids to migrate upward
 228 into Unit C, which also acts as a fluid reservoir. Here, magmatic fluids mix with marine and meteoric
 229 water (Caprarelli et al., 1997; Caliro et al., 2025). Bradyseism is primarily driven by the transient
 230 connection between reservoirs hosted in Units A and C, mediated by impermeable Unit B. Recently,
 231 Mantiloni et al. (2025) validated their analytical poroelastic solutions with Finite Element models,
 232 then used them as initial conditions to study surface displacement and pore pressure/stress changes
 233 from fluid flow between porous layers with different regimes. The episodic connection and
 234 disconnection between deeper and shallow reservoirs are sufficient to drive the ‘breathing’ mode. In
 235 Lima et al. (2025a and references therein) model, two processes operate on distinct and different
 236 timescales. The longer timescale, on the order of 10^3 – 10^5 years, is associated with magma cooling,
 237 solidification and production of lithostatically-pressured fluids, during which the brittle-ductile
 238 transition migrates to greater depths (see fig. 3 in Lima et al., 2025b). The shorter timescale, ranging
 239 from 1 to 10^2 years, is episodic in nature and linked to fluid migration and transient fracture
 240 propagation aided by increasing effective stress within the impermeable Unit B. Ground deformation

241 and seismicity are thus driven by fluid pressurization in the underlying reservoir leading to uplift,
 242 with subsidence caused by fluid depressurization following brittle failure and enhanced fracture
 243 permeability that allows the trapped overpressured fluids to escape and migrate upwards. The closing
 244 of the system occurs mostly by mineral deposition and relaxation after pressure release that closes
 245 the fractures and locally decreases permeability. So far, no model, including one recently proposed
 246 by Vanorio et al., 2025, has been able to explain the so-called mini events (Fig. 3) represented by
 247 interannual fluctuations that occur both during the multidecadal subsidence and uplift phases. An
 248 explanation of these neglected mini-events is one of the goals of this study: the correlation of these
 249 mini-events with the record of rainfall and aquifer recharge.

250

251 **3. Subsurface geology at CF: origin of the earthquakes and fluid circulation**

252

253 A fundamental step for reconstructing the fluid circulation in the CF region consists in characterizing
 254 the location and lateral extent of the relatively permeable and impermeable stratigraphic successions
 255 and the structures, folds and faults, in the area of interest. The east–west geological section across the
 256 CF region (Fig. 4) allows the identification of the main geological units that characterize the area,
 257 which are described below from bottom to top. A melting zone, affecting both the crystalline
 258 basement and the carbonates of the faulted Apennine thrust belt units (indicated as the substrate in
 259 Figs. 1c and 4) is covered by an irregular impermeable zone (carapace), formed by crystallized
 260 magma.

261 The substrate is covered by Unit A. The lower boundary of Unit A is an irregular surface, with a
 262 shape similar to the top of the carbonate unit outcropping along the Sorrento Peninsula, as confirmed
 263 by tomographic data showing seismic velocities exceeding 5 km/s at approximately 4 km depth (De
 264 Landro et al., 2025). Indeed, the thickness of Unit A is controlled by the Lower Pleistocene faults,
 265 forming a graben in the central part of CF, as shown in Fig. 4a. This structure corresponds to the
 266 NW-oriented grabens, such as those that crop out on the Sorrento Peninsula and the one that is buried
 267 in the northern Campanian Plain (Fig. 1). Unit A consists of continental and shallow-water
 268 sedimentary deposits that reach a thickness of 1.5 km based on Trecase and Cancelllo boreholes and
 269 is comprised of a succession of sands and silts interlayered by conglomerates and mudstone and acts
 270 as a permeable fluid reservoir (Fig. 4b).

271 A relatively thin clay-rich Unit B lies above Unit A, forming an impermeable unit with a large
 272 regional extent. Seismic lines located on the eastern margin of the Penta Palummo (PP, Fig. 1b) area
 273 support this interpretation. Fig. 5b shows a north–south multichannel seismic reflection profile that
 274 crosses an area where the pyroclastic deposits are absent (Fig. 5a). The interpretation of the profile,
 275 based on cross-correlation of densely spaced seismic profiles acquired in Naples Bay (e.g. Milia and
 276 Torrente, 2011), reveals a high amplitude, low frequency and continuous reflector corresponding to
 277 Unit B, between Unit A and the overlying Unit C. The seismic section (Fig. 5b) shows continuous
 278 parallel reflectors for Unit C, whereas Unit A is marked by continuous parallel reflectors in the
 279 southern part and by scattered high-amplitude reflectors towards the north. This latter seismic facies
 280 suggests the presence of fluids in the sediments. Since these facies are confined to Unit A, it
 281 demonstrates that Unit A is a fluid reservoir sealed by Unit B which prevents the upward migration
 282 of the fluids. This interpretation is supported by the findings in the Mofete 5 borehole that identified
 283 two aquifers at depths of 1600–1960 m and 2310–2699 m, separated by the impermeable layer
 284 corresponding to Unit B (Mf5, Figs. 2a and 4) and by the presence of an aquifer in the CF23 borehole
 285 at depths of 1445–1712 m (Fig. 4; Carella and Guglieminetti, 1983; AGIP, 1987).

286 Unit C is a regressive marine succession composed mainly of silts and sands, with interbedded
 287 lavas and volcanic deposits related to the earliest volcanism along the Campanian Margin. Due to its
 288 lithological characteristics, Unit C corresponds to a relative permeable unit (Reservoir C, Fig. 4).

289 A relatively thick pyroclastic unit, Unit D, overlies Unit C in the Pozzuoli area and corresponds
 290 to the pyroclastic, ignimbrites and volcanoclastics deposited over the last 100 ka (e.g. Milia and
 291 Torrente, 2011). This unit is characterized by low permeability due to welding, grain size variability,
 292 and post-depositional alteration and mineralization and can be considered a relatively impermeable
 293 unit. The pyroclastic unit presents a wedge external form, thickening toward the north, where it
 294 reaches a depth of approximately 2.5 km in the S. Vito borehole (Fig. 1c), and pinches out toward the
 295 west (Fig. 4). It is important to note that the lower boundary of the pyroclastic Unit D varies from
 296 about 2.5 km in the San Vito borehole to about 1 km below Pozzuoli, to about 0.5 km in the middle
 297 of Pozzuoli Bay, and disappears (or is present only in thicknesses of a few meters or as tephra) west
 298 of Pozzuoli (Milia and Torrente, 2011). Consequently, Reservoir C is only bounded upward by an
 299 impermeable unit where the pyroclastic wedge is present, thus representing a localized reservoir. This
 300 wedge architecture and the deepening of the base toward the faults (Fig. 1c) reflects the late
 301 Quaternary syn-ignimbrite fault activity (Milia, 2000; Milia and Torrente, 2011). The uppermost part
 302 of the succession comprises the younger Neapolitan Yellow Tuff deposits and alluvial sediments
 303 onshore, and marine silts and sands in Pozzuoli Bay (Fig. 4).

304 In areas where Unit D is absent, fluids circulating in Unit C can migrate upward to the sea floor,
 305 forming pockmarks as shown in Figs. 4 and 5c. The seismic section of Fig. 5c illustrates vertical
 306 features with transparent facies at depth terminating at the seafloor as chaotic facies and irregular
 307 topography, these features are characteristic of fluid migration pathways.

308 From the tectonic point of view, over the last 8 ka the CF/Pozzuoli Bay area has been
 309 characterized by active tectonics. In particular, the architecture of the sedimentary succession
 310 revealed a major fold, with an anticlinal culmination beneath Pozzuoli and a syncline beneath
 311 Pozzuoli Bay, formed in response to a local transpressive deformation (Milia and Torrente, 2000;
 312 2003). The folding reflects positive inversion tectonics due to the reactivation of pre-existing normal
 313 faults. During tangential-longitudinal strain folding, extensional faults and fractures form along the
 314 anticline crest and syncline troughs to accommodate the tectonic deformation (Figs. 2d, 6b; Ramsay,
 315 1967).

316 The Solfatara structure is a maar/diatreme system formed during a phreatic eruption ~4 ka ago,
 317 with faulting extending to ~2 km depth (Cipriani et al., 2008; Marini et al., 2022). This area exhibits
 318 intense faulting aligned with regional tectonic trends (e.g. Bruno et al., 2007). The highly fractured
 319 zone between Solfatara and Pozzuoli, particularly the diatreme itself, can be interpreted as a crestal
 320 collapsed structure atop the anticline (Figs. 4 and 6c).

321 The distribution of earthquakes is consistent with the reconstructed structure. Indeed, the
 322 earthquakes are concentrated at about 1–2 km depth beneath the anticline, while deeper events
 323 offshore lie between 2–4 km beneath the syncline (Figs. 4 and 6a) (cf. Tan et al., 2025). Seismicity
 324 is linked to ongoing folding, with fractures developing both above and below the neutral surface of
 325 the fold (Fig. 6b and 6c) (Ramsay, 1967) and in association with tectonic faults. Numerous micro-
 326 earthquakes affect the area (Fig. 6) especially in the intermediate zone between the anticline and
 327 syncline between depths of 1–2 km and upward in the Pozzuoli/Solfatara area. These micro-
 328 earthquakes can be attributed to the fractures generated by the fluid overpressure in Reservoir C and
 329 in the hinge zone of the anticline. Furthermore, according to the development of an inversion tectonic
 330 structure in a local transpressive regime, the focal mechanisms show transcurrent and oblique motion
 331 along faults-oriented NW, SE, NE, SW, EW, and NS, and the coexistence normal and reverse faulting
 332 (Milia and Torrente, 2003; Natale et al., 2024; Tan et al., 2025).

333 The reconstruction of stratigraphic and structural features, as illustrated in the geologic section
 334 shown in Fig. 4, is used for reconstructing the fluid circulation system, as illustrated in Fig. 4b. From
 335 the stratigraphic perspective, we can identify two relatively first-order impermeable levels: (1) Unit
 336 B, extending over the entire Campanian Margin at a depth of approximately 2 km in the Pozzuoli
 337 area; and (2) the pyroclastic units (Unit D), with a limited extension, at a depth of 0.5–1 km in the
 338 Pozzuoli area and thins to the west and terminates in Pozzuoli Bay. Two thick reservoirs are present
 339 between the impermeable units. Under Pozzuoli city, Unit A represents the reservoir for the fluids
 340 released from the deeper crystallizing magma and is separated from overlying units by impermeable
 341 Unit B. Unit A is subject to overpressure conditions until Unit B fractures, allowing fluids to escape
 342 upwards (Lima et al., 2025a, and references therein). The shallower Unit C represents a meteoric
 343 fluid reservoir and is present only where it is overlain by the pyroclastic wedge. A large-scale fracture
 344 permeability affects the area and allows fluids from Reservoir A to migrate upwards to Reservoir C,
 345 where the fluids mix and eventually escape to the surface in the Solfatara/Pisciarelli area along
 346 localized tectonic faults.

347 The reconstructed water circulation model (Fig. 4b) indicates that meteoric water falling on the
 348 CF accumulates under the Pozzuoli-Solfatara area. On the western side, under Pozzuoli Bay, sea
 349 water mixes with underground fluids, migrating both laterally and vertically, forming pockmarks on
 350 the flanks of the syncline in Pozzuoli Bay where the fluids reach the seafloor (Fig. 4). Mixed fluids
 351 (meteoric, marine, and magmatic) from different depths migrate upward through the fractures at
 352 Solfatara, as reported by several studies (Caprarelli et al., 1997; Caliro et al., 2025). The fluid
 353 circulation pattern illustrated in Figure 4b is consistent with the isotherm reconstruction proposed by
 354 Petrillo et al. (2013). In the western portion of the section, the isotherms descend into the basin,
 355 indicating lower temperatures compared to the eastern sector near the Pozzuoli-Solfatara area. Here,
 356 the isotherms rise, reflecting higher temperatures along the interface between Unit C and Unit B. The
 357 influx of cold meteoric fluids from inland areas into Unit C, combined with the influence of seawater
 358 in the bay, where Unit D is absent, causes the isotherms to be depressed to greater depths. Conversely,
 359 the ascent of hot fluids along major fracture zones, particularly along faults that extend to great depth
 360 near the top of the anticline, results in a sharp upward deflection of the isotherms (Fig. 4b).

361

362 4. Model to evaluate rainwater accumulation

363

364 At CF, rainwater can infiltrate into the subsurface through intense fracturing and is likely to
 365 accumulate primarily within Unit C. This accumulation increases both underground pore pressure
 366 and the pressure generated by the convective movement of hot water and pressurized water rising
 367 through the system. These pressures reduce the effective stress that binds the rocks together,
 368 potentially allowing for ground movement and uplift of the overlying surface.

369
 370
 371

The magnitude of this uplift depends on three main factors: (1) the volume of infiltrated water;
 (2) the compressibility and poroelastic properties of the surrounding rocks; (3) the magnitude of
 lithostatic confined pressure beneath the impermeable layer.

372
 373
 374
 375
 376
 377
 378

Geothermal activity can amplify the uplift through thermo-poroelastic effects. The resulting
 increase in pore pressure and ground deformation may induce earthquakes via two primary
 mechanisms: (1) When pore pressure surpasses the tensile strength of the rock, new fractures can
 form, releasing stress suddenly and generating small earthquakes; (2) Elevated pore pressure can
 reduce frictional resistance along pre-existing faults. This process — known as fault reactivation —
 can destabilize critically stressed faults and cause sudden slips that trigger earthquakes, especially in
 zones with significant water infiltration (Casertano et al., 1976; Bonafede and Mazzanti, 1997;

379 Siniscalchi et al., 2019; Guerriero and Mazzoli, 2021, and references therein; Wang and Manga,
 380 2021).

381 Rainwater at CF discharges through surface runoff, evaporation, and underground percolation,
 382 eventually reaching the sea. Figure 4b shows a geologic section across Campi Flegrei–Pozzuoli Bay,
 383 illustrating meteoric water circulation. It also shows the modelled subsurface path and accumulation
 384 of rainwater within Reservoir C (see section 2.1).

385 We hypothesize that rainwater falling more than 6 km from Rione Terra does not contribute to
 386 the aquifers beneath Pozzuoli, as it is likely diverted by the main fault encircling CF (Fig. 2a). Several
 387 highly fractured areas within CF, such as the Astroni crater (Fig. 2b and Fig. 4), may serve as major
 388 recharge areas. Tectonic or seismic activity can alter these fractures — sealing or opening them —
 389 and consequently modulate water recharge and discharge rates. A reduction in these rates leads to a
 390 change in meteoric water accumulation in Reservoir C (Fig. 4). In addition, groundwater infiltration
 391 is also influenced by variations in rainfall intensity. The seawater contribution is considered
 392 approximately constant.

393 The aim of our model is to determine whether interannual to multidecadal changes in rainfall
 394 amounts are correlated with the vertical surface displacements observed in the uplift zone centered
 395 around Pozzuoli (GNSS Rite Station). Detecting a correlation across multiple timescales (cf. Scafetta
 396 et al., 2004) between the uplift and rainwater accumulation would suggest that the impermeable
 397 stratum Unit D is affected by pressure changes due to: (1) vertical movement of the deeper Unit B
 398 pushed upward by inflation of Reservoir A, as already suggested in Lima et al. (2025, and references
 399 therein); (2) expansion of Reservoir C (region Eb in Fig. 4) where meteoric water can accumulate in
 400 the region above the anticlinal structure (Fig. 6).

401

402 4.1. Inverse approach to assess the local hydraulic conductivity

403

404 The creation of a hydrogeological model requires knowledge of the hydraulic conductivity of the
 405 strata in the CF area. This knowledge is not known *a priori*. In fact, envisioning a physics-based
 406 reductionist approach in which all known physical processes are considered to compute an output, is
 407 impractical due to the excessive number of unknowns.

408 The conversion of hydraulic conductivity (K) to the intrinsic permeability (k), a property of the
 409 rock matrix independent of the fluid properties and dynamics, depends on the saturation level of the
 410 medium as well as the dynamic viscosity and density of the fluid occupying the pore (or fracture)
 411 network. For a fluid saturated medium $K = \frac{\rho \vec{g}}{\eta} k$. For water near the surface, the factor converting
 412 intrinsic permeability to the hydraulic conductivity is $\approx 9.1 \times 10^{-8}$. However, under more realistic
 413 hydrothermal conditions, for example 350 °C and about 70 MPa (700 bars) at a depth ~ 3 km, the
 414 ratio $\frac{\eta}{\rho}$ is a factor of 7 larger compared to shallow groundwater. However, in our case, the lithology
 415 of the area is highly fractured and, therefore, it is not possible to derive the hydraulic conductivity
 416 from general hydrothermal conditions. Hence the use of hydraulic conductivity provides a mean-field
 417 description that includes variations in fluid properties and medium anisotropy and heterogeneity (e.g.,
 418 dependence of k on depth and lithology), which could be eventually used to find an effective intrinsic
 419 permeability (Bear, 1972).

420 The construction of an empirically based hydrogeological model starts by examining the data. It
 421 is observed that both the rainfall record and the ground vertical displacement record exhibit

422 significant interannual fluctuations that appear to be correlated with a time lag of a few years. Based
 423 on this observation, it is hypothesized that rainwater falling on CF infiltrates in an underground core
 424 reservoir located under Pozzuoli and affects the vertical movement. Since the hydraulic conductivity
 425 of the ground is a free parameter of our model, the hydraulic conductivity value is randomly varied
 426 within a range of values that the literature considers realistic for highly fractured igneous and
 427 metamorphic rocks (Freeze and Cherry, 1979) until a reasonable single value is found that could
 428 replicate the observed time lag between the interannual fluctuation observed in the rainfall record and
 429 in the ground vertical displacement record. We notice that the hydraulic conductivity, which is a
 430 velocity, depends on other parameters such as the intrinsic permeability, the viscosity, the fluid
 431 density and the temperature. However, for our purpose we ignore this complexity and simply estimate
 432 a reasonable hydraulic conductivity derived empirically from the observations.

433 In this way, the modeling automatically accounts for the observed time lag between rainfall and
 434 underground recharge, as water percolates through fractured upper crust of variable lithology to reach
 435 the reservoir under Pozzuoli. This enables a comparison between the rainfall record and the vertical
 436 ground movement in Pozzuoli since 1985, allowing us to examine whether the small interannual
 437 fluctuations (mini ups and downs), along with decadal and longer modulations of the two signals, can
 438 be correlated.

439 A double correlation observed at both interannual, and longer time scales provides stronger
 440 evidence that rainwater contributes to vertical ground movement, offering in addition a reasonable
 441 quantitative estimate — at least a lower bound — of this contribution and shedding light on the
 442 possible dynamics of the process. With the help of the model, it is possible to show that the higher
 443 limit depends on the drainage time scale of groundwater from the core reservoir (in Unit C) to the sea
 444 (Fig. 4).

445

446 *4.2. Rainfall data*

447

448 The proposed model uses the average daily precipitation dataset from ERA5 (Hersbach et al., 2020)
 449 to estimate rainfall over the CF region. Specifically, we sourced the daily dataset of rainfall reported
 450 in mm/day labeled “ERA5 1950-now 0.25° Europe” from the KNMI Climate Explorer (available at
 451 <https://climexp.knmi.nl/>, accessed on April 8, 2025). The ERA5 precipitation records are estimated
 452 averages provided on a $0.25^\circ \times 0.25^\circ$ grid. Consequently, we focused on the area bounded by
 453 longitudes $13.875^\circ\text{E} - 14.375^\circ\text{E}$ and latitudes $40.625^\circ\text{N} - 41.125^\circ\text{N}$, centered at $14.125^\circ\text{E} -$
 454 40.875°N . This selected region closely encompasses Rione Terra in Pozzuoli (approximately 14.12°E ,
 455 40.82°N), the site of the GNSS station Rite operated by the OV-INGV. Notably, this location
 456 corresponds to the CF area of maximum ground deformation and uplift.

457 The data of vertical displacements at GNSS Rite Station located in Rione Terra in Pozzuoli and
 458 depicted in Fig. 3 are taken from the Bulletins of the OV-INGV
 459 (<https://www.ov.ingv.it/index.php/monitoraggio-e-infrastrutture/bollettini-tutti/boll-sett-flegrei>) and
 460 from the supplementary of Bevilacqua et al. (2024).

461

462 *4.3. Model*

463

464 This section presents a mathematical framework for a hydrogeological model describing the
 465 dynamics of the underground rainwater percolation system beneath CF (Fig. 4). For this purpose, the
 466 surface inside the CF area has been divided into three concentric areas (Fig. 2b). We did not consider
 467 regional contributions because the tectonic structure of the CF caldera should be mostly bypassed by
 468 external flows (Fig. 2a). The model postulates that the vertical displacement observed at Rite Station,
 469 which is the area with the highest unrest, situated in Rione Terra, results from two distinct
 470 components:

471

$$472 \quad H_{B+C}(t) = H_B(t) + H_C(t) \quad (1)$$

473

474 where $H_B(t)$ represents the vertical displacement of the deeper Unit B, located approximately 2 km
 475 below the surface, and $H_C(t)$ denotes the vertical enlargement of the more superficial Unit C, situated
 476 at a depth of approximately 1-2 km between Unit B and the impermeable Unit D. Unit B plays two
 477 roles in this process. On the one hand, it prevents deeper fluids from Unit A from continuously rising
 478 upwards to more shallow depths, and on the other hand it prevents meteoric water from migrating
 479 downward into the deeper parts of the CF system.

480 The expansion of Unit C is primarily attributed to meteoric water accumulation, which
 481 predominantly varies with the volume of meteoric water falling over the CF region minus the
 482 discharge. Conversely, the vertical displacement of Unit B is assumed to be influenced by variations
 483 in the deep lithostatic pressure as explained by the magmatic hydrothermal model of Lima et al.
 484 (2025a, and references therein).

485 The schematic model presented below integrates the influences of precipitation, percolation, and
 486 flow dynamics within a hypothesized system of concentric buffers centered at Rione Terra, the point
 487 of maximum soil uplift in Pozzuoli (Fig. 2a and 2b). These processes are hypothesized to modulate H_C
 488 (t). Note that $H_B(t)$ cannot be independently quantified by our model, as the factors driving its
 489 dynamics remain unknown. Likely, $H_C(t)$ mostly determines the low amplitude and high frequency
 490 component of $H_{B+C}(t)$, whereas $H_B(t)$ may be responsible for the high amplitude and low frequency
 491 component of the vertical displacement observed at Rite Station (Rione Terra, Pozzuoli). However,
 492 some couplings may also be possible. Consequently, we infer various scenarios by analyzing and
 493 comparing the dynamical patterns of vertical displacements recorded at the Rite Station alongside
 494 variations in water accumulation developing in Unit C, estimated through rainwater amount changes
 495 resulting from variations in precipitation temporal patterns.

496 The region is conceptually divided into three concentric buffers, defined by radii R_0 , R_1 and R_2 ,
 497 by taking into consideration only the land side (Fig. 2b).

498 Thus, the proposed model speculates three ideal buffers derived from the CF tectonic geometry
 499 and its faults (Figs. 2a and 4) that regulate the meteoric water infiltration falling on the region. This
 500 geometry is inspired by the observation that (1) the CF area has a radius of about 6 km from Pozzuoli
 501 (second buffer), (2) the vertical ground movement is maximum around Pozzuoli in the center of the
 502 circles shown in Fig. 2b (model core) and (3) that the maximum fracturing of the ground occurs
 503 within 3 km from Pozzuoli (first buffer) where the highest seismic activity occurs (Figs. 2a and 6a).
 504 We verified that the model's results are not significantly influenced by these assumptions.

505

506 • **Model core:** This core is assumed to be located beneath Rione Terra at a depth h between 1 and 2
 507 km and with a radius of $R_0 = 1$ km. This core receives most of the meteoric water falling over the
 508 area within the ring faults at 6 km radius, leading to maximum ground deformation. Water from this
 509 core can only be discharged mostly into the sea over a time scale $\tau(t)$, which varies based on the
 510 permeability by fractures that could be influenced by very slow deformation associated with local
 511 tectonic activity as previously discussed.

512 • **First water buffer:** The model core is surrounded by the first buffer extending to a radius $R_1 = 3$
 513 km, including the highly fractured Solfatara area (Fig. 2b). This highly fractured area allows meteoric
 514 water to rapidly percolate and rapidly reach the model core at speed $V_1(t)$ that may vary with seismic
 515 activity.

516 • **Second water buffer:** This is the external buffer with a radius $R_2 = 6$ km (Fig. 2b). This area is
 517 less fractured than the first two as we consider only the on-land side, resulting in a slower percolation
 518 rate, $V_2(t)$.

519

520 For this hypothesized model, it is assumed that rainfall is uniformly distributed across the entire
 521 region. The infiltration speeds $V_1(t)$ and $V_2(t)$ may change over time because the area is seismically
 522 active, and the faults may evolve by changing the rate at which the water may infiltrate. Besides this
 523 dynamic, we assume that the infiltration rates represent an average speed in each area without, for
 524 example, differentiating between horizontal and vertical movement, which are expected to be
 525 characterized by different hydraulic conductivity values. Finally, upon reaching the model core, the
 526 water can only be discharged mostly into the sea with a time scale ($\tau(t)$), which can again vary over
 527 time because of the seismic activity of the area.

528

529 4.4. Rainfall contributions

530

531 The surface extension areas where rainwater falls of the three buffers are:

532

$$533 \quad \begin{aligned} A_{\text{core}} &= \pi R_0^2 \\ A_{\text{first buffer}} &= \pi R_1^2 - \pi R_0^2 \\ A_{\text{second buffer}} &= \pi R_2^2 - \pi R_1^2 \end{aligned} \quad (2)$$

534

535 Rainfall contributes to water inflow in the model core as follows.

536

537 4.4.1 Rainfall directly over the model core

538

539 Rainfall directly above the area A_{core} infiltrates vertically through the ground with a delay:

540

541 $t_{\text{delay,core}} = \frac{h}{V_1(t)}$ (3)

542 where h is the depth between 1 and 2 km. The daily contribution at time t to the core's water volume
543 from this area is:

544

545 $V_{\text{rain,core}}(t) = \frac{\alpha}{2} P(t - t_{\text{delay,core}}) \cdot A_{\text{core}}$ (4)

546

547 where: $P(t)$ is the rainfall rate and A_{core} is the central area of the core (πR_0^2). The factor 1/2 is adopted
548 because, according to the satellite photo of Fig. 2b about half of the area is covered by the sea. The
549 assumption is completed by considering that only a fraction α , generally less than 20%, of the
550 rainwater infiltrates. This fraction may vary over the entire region and, especially over the downtown
551 area of Pozzuoli, may be rather low because the surface is mostly paved. However, in our simplified
552 model we assume that the percolation fraction α is constant over the entire region. In this way the
553 fraction α is just a multiplicative factor that can be normalized out. We notice that even if the
554 rainwater contribution from the inner core, which mostly corresponds to the downtown of Pozzuoli,
555 is ignored ($\alpha = 0$) the result of our model would change by less than 3% because the area A_{core} is only
556 3% of the entire considered surface.

557

558 4.4.2. Rainfall over the first buffer

559

560 Rainfall over the first buffer area contributes to the model core through a percolation pathway, which
561 is supposed to be linear for simplicity. The delay is:

562

563 $t_{\text{delay,first}}(r) = \sqrt{\left(\frac{r}{V_1(t)}\right)^2 + \left(\frac{h}{V_1(t)}\right)^2}$ (5)

564

565 where r is the radial distance from the center. The corresponding daily contribution at time t to the
566 core's water volume from this area is:

567

568 $V_{\text{rain,first}}(t) = \frac{\alpha}{2} \int_{R_0}^{R_1} P(t - t_{\text{delay,first}}(r)) \cdot 2\pi r dr$ (6)

569

570 The factor 1/2 is again adopted because, according to the satellite photograph of the area (Fig.
571 2b) about half of the area is covered by the sea, and all water falling on the surface of this buffer is
572 assumed to percolate towards the core.

573

574

4.4.3. Rainfall over the second buffer

575

576 Rainfall over the second buffer flows linearly towards the first buffer and then continues to flow
 577 towards the model core. The depth at which water reaches R_1 is:

578

579
$$h_{\text{partial}} = h \cdot \frac{r-R_1}{r} \quad (7)$$

580

581 The total delay is:

582

583
$$t_{\text{total,second}}(r) = \sqrt{\left(\frac{r-R_1}{V_2(t)}\right)^2 + \left(\frac{h_{\text{partial}}}{V_2(t)}\right)^2} + \sqrt{\left(\frac{R_1}{V_1(t)}\right)^2 + \left(\frac{h-h_{\text{partial}}}{V_1(t)}\right)^2} \quad (8)$$

584

585 The daily contribution of rainwater at time t to the model core from this area is:

586

587
$$V_{\text{rain,second}}(t) = \frac{\alpha}{2} \int_{R_1}^{R_2} P(t - t_{\text{total,second}}(r)) \cdot 4 \arcsin(R_1/r) \cdot r \, dr \quad (9)$$

588

589 Eq. (9) assumes again the factor of 1/2 for the same reasons of above, but in addition it is assumed
 590 that only a portion of the meteoric water precipitating in this second area converges toward the model
 591 core. This portion decreases with the distance from the model core center as the arcsine function.
 592 Note that for $r = R_1$, $4 \arcsin(R_1/r) = 2\pi$ as in Eq. (6).

593

594 *4.5 Water flow dynamics*

595 4.5.1. Total inflow to the model core

596 The total daily inflow to the model core is the sum of the contributions across the three regions:

597

598
$$Q_{\text{in}}(t) = V_{\text{rain,core}}(t) + V_{\text{rain,first}}(t) + V_{\text{rain,second}}(t) \quad (10)$$

599

600 4.5.2. Outflow from the model core

601

602 The daily water outflow from the model core mostly through the fractures, is proportional to its
 603 accumulated water volume as

604

605
$$Q_{\text{out}}(t) = \frac{\text{Volume}_{\text{core}}(t)}{\tau(t)} \quad (11)$$

606

607 where $\tau(t)$ is the drainage timescale. For example, when the underground water more easily
 608 percolates through fractures, τ is smaller, while when the discharge is lowered by sealing of the
 609 fractures, τ is larger.

610

611 **4.5.3. Water volume at the model core and its vertical displacement**

612

613 The water volume in the model core changes dynamically as

614

615
$$\frac{d\text{Volume}_{\text{core}}(t)}{dt} = Q_{\text{in}}(t) - Q_{\text{out}}(t) \quad (12)$$

616

617 The water level in the model core, which is assumed responsible for some of the ground vertical
 618 movement, is proportional to

619

620
$$H_C(t) = \frac{\text{Volume}_{\text{core}}(t)}{A_{\text{core}}} \quad (13)$$

621

622 The equations delineate the mechanisms governing precipitation, percolation, and water flow within
 623 the considered CF area (Fig. 2b), which is made of two buffers at R_1 and R_2 characterized by different
 624 percolation speeds. This schematic model forms the basis for the subsequent numerical simulations.

625

626 **5. Data analysis and empirical modeling**

627

628 Figures 7a and 7b depict the daily rainfall measurements across CF since 1970, and their cumulative
 629 totals for each 1-year period. The multi-year smooth orange curve - obtained with the MATLAB
 630 function smooth, with Localized Scatterplot Smoothing (LOESS) = 0.2, which approximately
 631 corresponds to a moving average of 4 years - presented in Fig. 6b indicates a decline in annual rainfall
 632 from approximately 1300 mm/year in the 1970s to 950 mm/year by around 1995. The rainfall
 633 decrease during this period was followed by an increase in rainfall between 1995 and 2010–2015,
 634 peaking at approximately 1250 mm/year, before stabilizing at an average of 1125 mm/year during

635 the period spanning from 2019 to 2025. Furthermore, Fig. 7b illustrates interannual fluctuations
 636 characterized by recurring peaks, a climatic phenomenon commonly associated with the El Nino
 637 Southern Oscillation (ENSO) and the Northern Atlantic Oscillation (NAO) systems. Four of these
 638 prominent peaks (high amount events) are identified with red markers labeled A, B, C, and D.

639 Fig. 7c illustrates the vertical displacement recorded at the GNSS Rite Station. The rapid uplift
 640 observed during the 1984–1985 unrest, attributed to the uplift of Unit B shown in Fig. 4, was followed
 641 by a gradual subsidence totaling approximately 0.93 m, which persisted until 2004–2005.
 642 Subsequently, beginning in 2005, a monotonic and accelerating uplift is observed, which exceeded
 643 about 1.4 m in January 2025 (Bulletins of the OV-INGV, 2025). Fig. 7d presents the detrended
 644 vertical displacement, isolating its smooth component represented by the orange curve in Fig. 7c. Fig.
 645 Fig. 7d identifies multiple interannual mini uplifts with an amplitude of about 4–5 cm. The four largest
 646 uplifts are denoted in the figure by letters A, B, C, and D (corresponding to the high rainfall events
 647 of Fig. 7b).

648 A visual comparative analysis of the graphs in Fig. 7 suggests a correlation between the
 649 multidecadal variations in annual rainfall (Fig. 7b) and the gradual vertical displacement observed at
 650 the GNSS Rite Station from 1985 to the present (Fig. 7c), with an approximate time-lag of 10–15
 651 years from 1985 to about 1990–1995 and then increases until 2010–2015. Additionally, a comparison
 652 between the interannual fluctuations depicted in Fig. 7b and 7d shows a lagged correspondence,
 653 particularly for the four major peaks labeled with red letters A, B, C, and D in both graphs. This
 654 alignment occurs when accounting for a time-lag of approximately 4 years for peaks A and B, and
 655 around 3 years for peaks C and D. This correspondence suggests that changes in rainfall patterns may
 656 have contributed to the ground vertical movement shown in Fig. 6c with time-lags of 4 and 3 years,
 657 respectively, because of the percolation times required by the meteoric water to reach the model core.
 658 After 2010 a 3-year time lag could indicate increased fracturing which facilitates rainwater
 659 percolation.

660 The graphs in Fig. 7d also show actual rainfall and vertical displacement data and the lagged
 661 correlation between rainfall patterns and CF ground uplift and multidecadal unrest is highlighted.
 662 Here, we propose an empirical model that aims to recreate this time lag between the rainfall record
 663 and the underground water accumulation function by simulating a simple hydrological flow model
 664 as described above.

665 The model incorporates several free parameters. The choice of the best approximate values of
 666 these parameters was done by a Monte Carlo method of running the model several times by changing
 667 the parameter values to obtain a good configuration that correlates the model outputs with the patterns
 668 of the vertical displacement at the GNSS Rite Station (Fig. 7c).

669 The main free parameters of the model were chosen as: $R_0 = 1$ km, $R_1 = 3$ km, and $R_2 = 6$ km, for
 670 the three concentric areas shown in Fig. 2b; $h = 2$ km depth; $V_1 = 4$ m/day (hydraulic conductivity)
 671 until 1996 and then it is assumed to gradually accelerate as a parabola to $V_1 = 5$ m/day in 2025; and V_2
 672 $= \frac{2}{3}V_1$ because we assumed that the second buffer is less fractured than the first one (Fig. 2b).

673 The above hydraulic conductivity values are empirically assessed because the actual values in CF
 674 are unknown and, in any case, the actual hydraulic conductivity is highly variable because of the
 675 anisotropy of the permeability in CF area. In any case, a hydraulic conductivity of 4–5 m/day suggests
 676 that groundwater flows at an average speed of approximately 5×10^{-3} cm/s, or about 1.6 km/year.
 677 This flow rate is reasonable because it is typical in scenarios involving highly fractured igneous and
 678 metamorphic rocks, where hydraulic conductivity can reach values as high as 3×10^{-2} cm/s,
 679 corresponding to about 10 km/year (Freeze and Cherry, 1979). The model mean-field hydraulic
 680 conductivity from our model can be converted to an intrinsic permeability using the properties of the

681 fluid. A hydraulic conductivity of 4 m/day is equivalent to an intrinsic mean-field medium
 682 permeability of 4×10^{-12} m² for an aqueous fluid (assumed pure H₂O) at 1 bar and 25 °C and $5.8 \times$
 683 10^{-13} m² for an aqueous hydrothermal fluid at 700 bars (~3 km depth) and 350 °C. These estimated
 684 mean-field intrinsic permeabilities are consistent with weakly consolidated Quaternary marine and
 685 continental deposits and fractured volcanic and volcanoclastic lithologies in the shallow crustal
 686 section near Pozzuoli (Judenherc and Zollo, 2004; Milia and Torrente, 2020). The hydraulic
 687 conductivity V_1 is assumed to gradually accelerate from 4 to 5 m/day to reproduce the time lags of 4
 688 and 3 years observed in Fig. 7d. The acceleration of the hydraulic conductivities (V_1 and V_2) could
 689 be explained by the observed increasing seismicity indicative of an enhanced local fracture
 690 permeability. High Gutenberg-Richter 'b' values of 1.3–1.7 in the earthquake swarm scaling relation
 691 $\log N = a - bM$ (N is the cumulative number of earthquakes with magnitude larger than M and a and
 692 b are constants) at depths above 3 km is consistent with fracture-aided fluid migration in this region
 693 (Glazner and McNutt, 2021; Tramelli et al, 2024).

694 Figure 8 shows the results obtained with the model described above under two drainage
 695 conditions (Model case #1 and Model case #2), as detailed below. The adopted two cases were useful
 696 because Eq. (1) has two different components (H_B and H_C), while the model is supposed to simulate
 697 only H_C . For this reason, we run the model for two extreme cases for the drainage timescale (τ), as
 698 detailed below.

699 Fig. 8 (left) shows the results obtained using Models case #1 that assumes that the drainage
 700 timescale is constant as $\tau(t) = 1$ year. Fig. 8 (right) shows the results obtained using Models case #2
 701 that assumes that the drainage timescale is variable as: $\tau(t) = 1$ year until 1985 (just after the 1982–
 702 1984 unrest), then it decreases parabolically in time until $\tau(t) = 0.5$ year in $t = 2007$ (when the first
 703 mini uplift occurred after the beginning of the new uplift phase in year 2005) and finally to rise again
 704 parabolically until $\tau(t) = 1.5$ year in the year $t = 2025$ (Fig. 7c).

705 The drainage timescale, $\tau(t)$, represents the temporal scale over which underground water is
 706 discharged into the sea. A larger $\tau(t)$ corresponds to increased accumulation of water within Unit C.
 707 In Model case #1, when $\tau(t)$ is assumed to be constant, the estimated timescale is set to 1 year to
 708 approximately match the previously mean-field hydraulic conductivity of 1.6 km/year since Unit C
 709 is located about 1–2 km below the surface (Fig. 8a₁).

710 In Model case #2, $\tau(t)$ is assumed to change over time. During the subsidence period (1985–
 711 2005), $\tau(t)$ should have gradually decreased because the system opened to fluid circulation by
 712 fracture formation (Lima et al., 2025a and references therein). Conversely, during the uplift period
 713 (post-2007), $\tau(t)$ should have progressively increased as the uplift is a consequence of the closure of
 714 the system to fluid circulation (Fig. 8a₂).

715 The left and right panels of Fig. 8 show the results of the Model cases #1 and #2 run under the
 716 two discussed drainage scenarios: panels a₁ and a₂ report the model outputs given by Eq. (13) that
 717 provides the estimated underground water levels; panels b₁ and b₂ (which show the same graph for
 718 comparison) illustrate the vertical displacement recorded at the GNSS Rite Station; panels c₁ and c₂
 719 show the residual of the model outputs detrended to remove the smooth component; and panels d₁
 720 and d₂ (which show the same graph for comparison) show the residual of the vertical displacement
 721 shown in b₁ and b₂. The residual curves shown in Fig. 8 panels c₁ and c₂ reveal that the underground
 722 water rise function (Eq. (13)) exhibits interannual fluctuations that are strongly correlated with those
 723 observed in the vertical displacement recorded at the GNSS Rite Station. This relationship suggests
 724 that the observed mini uplifts (Fig. 3) may have been driven by variations resulting from fluctuations
 725 in underground water accumulation in Unit C (at approximately 1–2 km depth) beneath Pozzuoli.

726 The rainwater rise function (Fig. 8 panel c₁ and c₂) indicates that these water fluctuations have an
 727 amplitude of approximately 40–50 cm and are broadly consistent with the variations in vertical

728 displacement recorded at the GNSS Rite Station (panels d), which have an amplitude of about 4–5
 729 cm (Fig. 8 panel d₁ and d₂). This implies that to convert the vertical displacement with our empirically
 730 modelled water accumulation parameter H_C (Eq. (13)) we can use the conversion factor of roughly
 731 10.

732 By using this empirical conversion factor also for the multidecadal scale, we now proceed to
 733 examine the implications arising from the two scenarios related to the drainage timescale $\tau(t)$.

734 The Model case #1 illustrated in Figure 8a₁ indicates that the underground water level function,
 735 described by Eq. (13), increased by approximately 3 m from its minimum to its maximum. Using the
 736 conversion factor 10, 3 m corresponds to an estimated ~ 30 cm rise in the vertical displacement
 737 recorded at the GNSS Rite Station. Given that the total vertical displacement H_{B+C} from 2005 to
 738 January 2025 amounts to about 1.4 m, it can be inferred that $H_C \approx 0.3$ m and $H_B \approx 1.1$ m.
 739 Consequently, under the assumption that the drainage timescale remains constant over time, most of
 740 the uplift ($\sim 80\%$) observed at CF could be attributed to the uplift of deeper Unit B, located at a
 741 depth of approximately 3 km. In contrast, interannual changes to rainfall amount contributed to the
 742 minor interannual uplifts plus to roughly 20% of the total uplift from 2005 to 2025 by enlargement
 743 of Unit C, situated at a depth of about 1–2 km.

744 The statistical tests and their significance of the correlation between the modeled interannual
 745 groundwater accumulation fluctuations (blue curve in Fig. 8c₁) and the interannual variations in
 746 vertical displacement recorded at the GNSS Rite Station (Fig. 8d₁) are discussed in the Appendix.
 747 The Model case #2 presented in Figure 8a₂ suggests that the underground water level function (Eq.
 748 (13)) increased by approximately 12 m from its 2005 minimum to its 2025 maximum. This rise
 749 corresponds to an estimated ~ 1.2 m increase in the vertical displacement recorded at the GNSS Rite
 750 Station. Given that the total vertical displacement H_{B+C} from 2005 to January 2025 amounts to 1.4
 751 m, it can be inferred that $H_C \approx 1.2$ m and $H_B \approx 0.2$ m. Under the assumption that the drainage
 752 timescale varied over time as hypothesized above, most of the uplift ($\sim 86\%$) observed at CF could be
 753 attributed to the enlargement of Unit C, situated at approximately 1–2 km depth meaning that the
 754 underground accumulation of meteoric water contributed to the interannual mini uplifts plus nearly
 755 86% of the uplift from 2005 to 2025. Under this scenario, the contribution of Unit B to the overall
 756 uplift would be estimated as only $\sim 14\%$ of the total displacement.

757 It is, therefore, evident that the process is also highly sensitive to variations in the drainage
 758 timescale function $\tau(t)$. For instance, if $\tau(2025)$ is assumed to have risen to 1.7 years instead of the
 759 hypothesized 1.5 years, 100% of the total uplift would be attributed to underground water
 760 accumulation within Unit C. This extreme scenario may not be realistic since there is the need to
 761 explain why the drainage time scale should have increased during the last 20 years.

762 The two models indicate that fluctuations in precipitation over the past 40 years may have
 763 contributed to at least 20% of the total uplift (Model case #1) recorded at the GNSS Rite station
 764 between 2005 and 2025. However, considering the likelihood of a simultaneous increase in the
 765 drainage timescale (Model case #2) — potentially driven by heightened pressure beneath the closed
 766 Unit B — which could partially seal the drainage fractures, meteoric water may accumulate more and
 767 could have played a greater role in the total observed uplift. Thus, Unit B and Unit C may interact
 768 dynamically, as the uplift of Unit B could reduce drainage efficiency, leading to a longer timescale
 769 $\tau(t)$ and, therefore, to a major contribution of Unit C to the total uplift.

770

771 **6. Discussion**

772

773 The recent uplift of central Pozzuoli has been accompanied by shallower earthquake hypocenters
 774 compared to the 1982–1984 uplift episode (De Siena et al., 2017), indicating dynamic changes in the
 775 fractured system at depth. These changes are likely favored by additional rainwater infiltration into
 776 Unit C, which alters the hydrological loading rate and increases pore pressure, thereby enhancing
 777 seismicity. Elevated fluid pressure reduces the normal stress acting on fault planes and may exert a
 778 lubricating effect (e.g., Becken et al., 2011; Scuderi and Collettini, 2016, and references therein).
 779 Moreover, thermal expansion of pore fluids can further destabilize fault systems by decreasing
 780 effective stress across pre-existing zones of weakness, potentially triggering the numerous seismic
 781 swarms observed during the current phase of CF bradyseism (Guerriero and Mazzoli, 2021).

782 The schematic hydrodynamic circulation (Fig. 4) shows that it is strictly governed by the tectono-
 783 stratigraphic framework.

784 Subsequent meteoric fluid infiltration is linked to the ongoing stages of syn-folding fracturing.
 785 These folds are indicative of shallow-formed structures characterized by extensive networks of
 786 fractures and faults that enhance fluid mobility (Fig. 6c). This reconstruction has significant
 787 implications for understanding the dynamics of the area and forecasting future eruptions.

788 Based on the described stratigraphy, two main impermeable units define fluid-rich reservoirs
 789 located within Unit A and Unit C (Fig. 4). The key impermeable layer is Unit B that covers the entire
 790 region. Seismic reflection profiles reveal that fluid accumulates within Unit A (Fig. 5b). Critically,
 791 above Unit B, the seismic horizons are parallel and continuous, demonstrating that Unit B effectively
 792 seals the underlying reservoir (Unit A). This confirms that sedimentary Unit B represents an
 793 impermeable barrier within the stratigraphic framework of Naples Bay and Campi Flegrei.

794 Further confirmation is provided by two distinct aquifers encountered in the Mofete 5 borehole.
 795 These findings support the existence of a regional impermeable layer. In this context, Unit A, located
 796 between the carbonate basement and Unit B, acts as a fluid-rich reservoir subject to overpressure
 797 conditions. Numerous earthquakes beneath Pozzuoli Bay occur within this unit.

798 The upper impermeable unit is the pyroclastic wedge, which partially seals the Unit C reservoir
 799 until it extends beneath the bay of Pozzuoli, where Reservoir C is not constrained and the fluids reach
 800 the surface forming undersea pockmarks (Figs. 4 and 5c). Beneath the Pozzuoli–Solfatara area, this
 801 boundary between Unit C and the impermeable pyroclastic unit lies between 0.5 and 1 km depth.
 802 Summarizing, a critical distinction emerges between the reservoirs of Unit A and Unit C. Unit A is
 803 uniformly sealed by Unit B across the basin, while Unit C is only sealed where the pyroclastic wedge
 804 is present and where bradyseismic takes place. As illustrated in Fig. 4, in the absence of pyroclastic
 805 deposits above Unit C, fluids escape upward and discharge at the seafloor. This explains, along with
 806 the tectonic anticline formation under Pozzuoli Rite, why this area is affected by the maximum uplift.

807 Fig. 4 shows the reactivation of ancient normal faults during the deposition of pyroclastic wedges,
 808 particularly in the eastern part of the section. The tectonic event documented in Pozzuoli Bay over
 809 the last 8 ka (Milia and Torrente, 2000) corresponds to the formation of a syn-sedimentary fold,
 810 culminating in the Pozzuoli–Solfatara anticline — a highly faulted region where fault orientations
 811 follow regional tectonic trends (e.g., Bruno et al., 2007). In this context, tectonic inversion has folded
 812 the strata within zones bounded by reactivated normal faults.

813 The structural and stratigraphic permeability architecture critically influences fluid distribution
 814 and migration pathways (e.g., Sibson, 1996, 2003). These pathways generally involve downward
 815 percolation of meteoric and sea waters through fractures and upward movement of magmatic fluids.
 816 The depositional setting in which folds form governs a spectrum of fluid transport processes, with
 817 fluids driven from high- to low-pressure zones. Overall, deep hydrothermal systems are exceptionally
 818 water-rich, facilitating overpressure generation and fluid escape throughout the development of

819 antecedents. This results in diverse fluid migration structures — from deep to shallow — such as mud
 820 dykes, sills, laccoliths, volcanoes, fluid escape pipes, crestal normal faults, and thrust faults. Among
 821 these, crestal anticline faults play a major role in transmitting fluids to upper fold regions (Evans and
 822 Fisher, 2012).

823 Within Unit C, upward fluid migration through folded strata is likely reflected by the seismicity
 824 occurring at depths of 1–2 km below the pyroclastic wedge (Unit D, Fig. 4). Faults beneath the crestal
 825 anticline — Solfatara, Pisciarelli, and Agnano — reach depths of around 2 km (Fig. 6c), enhancing
 826 the pyroclastic wedge's permeability and enabling fluid escape from Unit C.

827 These fluids rise through faults and mix locally with shallow groundwater (Aiuppa et al., 2006).
 828 Volcano-tectonic discontinuities in this zone also promote vertical mixing among meteoric water,
 829 deep CO₂-rich fluids, and seawater.

830 Once again, the “hydrothermal model” explains how Unit B (Fig. 4), which is subject to
 831 compressive tectonic stress due to the anticline formation, governs bradyseism over timescales from
 832 1 to 100 years, acting as a valve between the hydrostatic and lithostatic systems. If fully sealed, Unit
 833 B could cause 40 m uplift (Lima et al., 2009). However, the fractured system prevents complete
 834 sealing, resulting in limited uplift or subsidence.

835 Connectivity between the two systems evolves cyclically through hydrothermal deposition of
 836 secondary minerals (reducing permeability) and fracture propagation (increasing permeability). This,
 837 along with the thermo-poroelastic properties of rocks (first advanced by Casertano et al., 1976), leads
 838 to alternating uplift and subsidence phases (Lima et al., 2025a, and references therein). Lima et al.
 839 (2025a) argue that in 2005, closure of fractures in Unit B and the increase in lithostatic pressure
 840 started both a new phase of ground uplift and a partial sealing of the fractures (by mineralization
 841 depositions, see: De Vivo et al., 1989; Belkin and De Vivo B., 2023; Belkin et al., 2023, 2024) and
 842 that the slower uplift velocity is due to the opening of new moderate fractures that allows the deep
 843 fluids to escape, reducing the pressure of magmatic fluid below the impermeable layer corresponding
 844 to Unit B (Fig. 4). These magmatic fluids would be released into the Reservoir C (Fig. 4b) as
 845 demonstrated by recent studies on the chemical-physical variations recorded in the Solfatara
 846 fumaroles (Caliro et al., 2025).

847 The present study complements previous research, taking into consideration the contribution of
 848 infiltrating meteoric water to the uplift of Pozzuoli Rite. The proposed model evaluates the infiltration
 849 of meteoric water under Pozzuoli and shows a correlation between the recharge of rainwater into the
 850 CF geothermal buffer and the uplift caused by the local bradyseism. Previous studies have identified
 851 correlations between rainfall events, tidal activity, and seismicity in the region (Palumbo, 1985;
 852 Mazzarella and Palumbo, 1989; Petrosino et al., 2018; Scafetta and Mazzarella, 2021) but not
 853 explicitly linked to the vertical ground movement. Those studies suggested triggering mechanisms
 854 due to meteoric and sea water infiltration as well as lunar and solar tidal effects. For instance, on
 855 March 13, 2025, the most significant seismic event in the past 40 years ($M = 4.6$, made up of two
 856 close earthquakes) coincided with a full Moon, several days of low atmospheric pressure in the
 857 Campanian Plain, and heavy rainfall. Rainfall, low atmospheric pressure, and tidal activity act as
 858 perturbing factors in a critically balanced system.

859 Petrosino et al. (2018) and Scafetta and Mazzarella (2021) observed that rainfall does not always
 860 trigger earthquakes at CF, nor are all seismic events necessarily caused by water infiltration. In fact,
 861 CF area is inherently seismically active due to bradyseism dynamics caused mostly by magmatic
 862 fluids being continuously released from the crystallizing magma (>7.5 km deep), with its
 863 crystallization front migrating downward (Fig. 4; Burnham, 1979; Lima et al., 2005).

864 Such magmatic fluids, at lithostatic pressure, are trapped at depth by the impermeable Unit B
 865 (Fig. 4), until the effective stress exceeds the fracture strength, creating low magnitude seismic
 866 events, and the transfer of fluids into Unit C.

867 The novelty of our study lies in analyzing long-term rainfall data (from 1950) using a simple
 868 hydrogeological model (section 5) to assess variations of meteoric water underground infiltration
 869 since at least 1985 correlated with the detailed tectonic stratigraphic reconstruction of CF volcanic
 870 system. The hypothesis of the model is that the CF system can be subdivided into three concentric
 871 areas with a central reservoir below Pozzuoli Rite that can accumulate infiltrated meteoric water
 872 because it has an anticline structure with two reservoirs constrained between two impermeable layers
 873 (Figs. 4 and 6), which do not allow the fluid to easily discharge causing an overpressure. For lack of
 874 data, only empirically average hydraulic conductivities for each area are considered. The estimated
 875 hydraulic conductivities, when converted to intrinsic permeability, are reasonably consistent with
 876 lithologies like those of CF area.

877 Morphologically, the CF region near Astroni-Solfatara is a seismically active highly fractured
 878 zone that serves as an efficient collector of meteoric waters (Figs. 4 and 6c). In particular, the Astroni
 879 crater is an area covering $\sim 2.5 \times 10^6 \text{ m}^2$ upstream Solfatara-Pisciarelli area (Fig. 2b), which contains a
 880 small lake of $\sim 5 \times 10^4 \text{ m}^2$ at its bottom. Another significant basin east of Solfatara is the Agnano crater
 881 ($\sim 3 \times 10^6 \text{ m}^2$), which hosted a volcanic lake ($\sim 10^6 \text{ m}^2$) until it was drained via channels constructed in
 882 1870. Additional craters, like Lake Avernus (Fig. 2b), are also found on the western side of Pozzuoli.
 883 Fig. 7b shows that the 365-day meteoric water amount function in the CF area presents interannual
 884 peaks every few years (which are indicated with the letters A, B, C, D). Fig. 7d shows, instead, the
 885 residual curve of the vertical displacement in Pozzuoli Rite Station (Fig. 7c). By comparing Fig. 7b
 886 and 7d, it is observed that the meteoric water amount function correlates well with the function
 887 describing the vertical displacement of the Pozzuoli area both at the decadal and interannual scales.
 888 In fact, rainfall amount decreased from the late 1970s to about 1990–1995 and then increases until
 889 2010–2015 and remained approximately constant until date (Fig. 7b). This pattern correlates well,
 890 with a time lag of 10–15 years with the vertical displacement decrease from 1985–2005 and the
 891 subsequent uplift until the present (Fig. 7c). Instead, the time-lag between the interannual mini-uplift
 892 peaks of rainwater amount is about 4 years prior to 2010 (Fig. 7d), then it decreases to about 3 years
 893 afterward, indicating an increase in hydraulic conductivity.

894 The proposed model was used to simulate if the infiltration of meteoric water in the reservoir of
 895 Unit C under Pozzuoli Rite can contribute to the observed uplift dynamics. To explain the observed
 896 lagged correlations shown in Fig. 7, we take into consideration that the rainwater accumulation also
 897 depends on a timescale $\tau(t)$ of discharge that could change in time because of the seismicity of the
 898 area. The model simulations are shown in Fig. 8. Here, we model two different cases: Model #1 uses
 899 a constant timescale $\tau(t)$ of discharge; Model #2 uses a variable timescale $\tau(t)$ of discharge. The
 900 increase in the timescale $\tau(t)$ of the drainage in Model #2 (Fig. 8 right) leads to an increase in the
 901 contribution of rainwater penetrating in Unit C to the total uplift.

902 The model simulations suggest that the interannual mini uplifts are related to the interannual
 903 variation of rainfall amount. For example, the strong mini uplift occurred in 1989 (point A in Fig. 7d)
 904 could have been triggered by the significant increase in rainwater between 1985 and 1987 (point A
 905 in Fig. 7b). The same lagged correlation of about 3–4 years between interannual rainwater maxima
 906 and all observed mini uplifts of about 4–5 cm is evident by comparing Fig. 7b and 7d, and the water
 907 processed signals in Fig. 8c₁ and 8c₂.

908 In fact, both Model cases #1 and #2 show that the interannual variations of the meteoric water
 909 infiltration within Unit C correlate well with all observed mini uplifts (Fig. 8c and 8d). The time-lag
 910 observed with the rainwater amount is covered by the percolation times that the meteoric water,
 911 falling on the land of CF area, needs to reach the model core under Pozzuoli Rite (Fig. 4, area “Eb”).

912 In summary, the results of this study (Fig. 8) indicate that an increase in rainwater infiltration has
 913 occurred from 2004–2005, likely along with Unit B sealing and the beginning of a new phase of
 914 ground uplift. We interpret that the total uplift is the combined contribution of both the fluid pressure,
 915 mostly of magmatic origin under the impermeable Unit B, and of meteoric water penetrating in Unit
 916 C under the impermeable pyroclastic Unit. Our Model #1 suggests that meteoric water accumulation
 917 under Pozzuoli Rite has contributed a minimum of 20% of the total uplift (Fig. 8a₁). Model 2, instead,
 918 implies a larger contribution to the total uplift of meteoric water accumulation in Unit C because it
 919 supposes that Unit B can control the fracturing of the system that can change the drainage timescale
 920 $\tau(t)$. In the present case, it is likely that $\tau(t)$ has increased since 2005 (Fig. 7c) when the uplift slowly
 921 started.

922 A final consideration is that tectonic events on a regional scale could have an impact on
 923 bradyseism. For example, the rapid uplift recorded between 1982 and 1984, when approximately
 924 1.80 m of ground inflation occurred in just two years, could have been a consequence of the 1980
 925 Irpinia earthquake of M 6.9 (Bernard and Zollo, 1989), located about 90 km from CF. It could be
 926 hypothesized that the latter triggered — within two years — fracturing of the crystallized carapace
 927 of the deep magma chamber with the release of magmatic fluids in Reservoir A (Fig. 4) causing an
 928 increase of lithostatic pressure acting as a powerful driver of unrest. Even the eruption of Vesuvius
 929 in 79 AD is thought to have been triggered — after a long repose time — by a regional earthquake
 930 that struck 15 years earlier (Morgan et al., 2006).

931

932 7. Conclusions

933

934 This study documents the contributions of fluids having diverse origins to drive ground deformation
 935 and seismic activity in the geologically and tectonically complex CF area of southern Italy.
 936 Specifically, this work suggests a direct dynamic link between multiscale temporal rainfall patterns
 937 and bradyseism in CF, Italy. This connection necessarily involves time-lags, as rainwater must
 938 percolate through subsurface layers to reach the accumulation core located beneath Pozzuoli, at
 939 approximately 1–2 km depth. This temporal delay has been hydrologically modeled and is consistent
 940 with the hydrogeologic properties of the sediments and lithologies underlying the region.

941 The observed shift in time lags — from about 4 years before 2010 to roughly 3 years afterward —
 942 between interannual fluctuations (mini uplifts of 4–5 cm), may indicate that the hydraulic
 943 conductivity slightly increased from 2005 to date, possibly resulting from enhanced intrinsic
 944 permeability due to increased fracturing caused by seismic activity associated with the accelerated
 945 uplift rate since 2010.

946 The multidecadal pattern of ground deformation, characterized by subsidence from 1985 to 2005
 947 followed by uplift since 2005, appears correlated with a similar variation in the rainfall record, with
 948 an estimated lag of around 10–15 years. The hydrological Model #1 estimates that about 20% of the
 949 1.4 m uplift since 2005 may be attributed to groundwater infiltration. However, this percentage could
 950 increase depending on the drainage efficiency determined by a variable timescale $\tau(t)$ of discharge,
 951 as demonstrated by Model #2.

952 The proposed model underscores the significant role of rainfall input in the current unrest and offers
 953 a quantitative framework for estimating its contribution. To mitigate uplifts and to keep constant the
 954 underground meteoric water level in Unit C below Pozzuoli we estimated that it is necessary to draw
 955 something of the order of 1000 m³ of underground water per hour.

956 Our results suggest also that a strategic mitigation measure could be to drain the surface meteoric
957 water at the CF area and, particularly, that falling inside the Astroni crater located upstream from
958 Solfatara–Pisciarelli. Historically, such an intervention would resemble the project carried out in the
959 Agnano crater in 1870, when surface water accumulation formed a lake. Today, the Solfatara–
960 Pisciarelli remains the most concerning area for public safety. However, the main benefits of such
961 intervention may become relevant only after a few years, due to the time required by the meteoric
962 water to percolate into Unit C below Pozzuoli. In any case, meteoric water may trigger the local
963 seismic activity within few days or weeks from rain events because infiltration of rainwater could
964 lubricate superficial faults (Scafetta and Mazzarella, 2021).

965 Fracturing at the apex of the anticline beneath the Solfatara crater is particularly intense, forming a
966 network of fractures that terminate at approximately 2 km depth, resulting in shallow seismic activity.
967 Conversely, in the Bay of Pozzuoli, fracturing at the syncline extends to greater depths, which gives
968 rise to deeper seismicity. Additionally, earthquakes with magnitudes equal to or greater than 4 are
969 concentrated along the main faults affecting the area and witness the reactivation of the preexisting
970 faults during the present tectonic activity. Finally, the tectono-stratigraphic architecture of the CF
971 area raises questions about the interpretation of the CF volcanic system as a caldera.

972

974

Appendix: Statistical test

975

976 To test the statistical significance of the observed correlation between the interannual water
 977 accumulation fluctuations (blue curve in Fig. 8c₁) and the interannual variations in vertical
 978 displacement recorded at the GNSS Rite Station (Fig. 8d₁) we adopt three methodologies:

979

9801. The direct Pearson linear correlation between the two curves depicted in Fig. 8c₁ and 8d₁ gives a
 981 correlation coefficient $R_o = 0.127$ that, for the 13,879 daily data from 01/01/1987 to 12/30/2024, gives
 982 a confidence probability of $P \ll 0.000001$, which means that the two curves are highly correlated.

9832. We use a Monte Carlo approach to test whether random rainfall records with mean and standard
 984 deviation equal to the real one could produce water accumulation curves with correlation results
 985 statistically compatible with that obtained using the real data, $R_o = 0.127$, which is assessed above in
 986 point 1. To accomplish this, we shuffle the original daily rain record to reproduce 1000 synthetic
 987 daily rain records with the same length of the original one. The random shuffling destroys the
 988 autocorrelation patterns observed in the data but conserves its mean and standard deviation of the
 989 record. Thus, the test can assess the correlation relevance of the specific dynamics present in the
 990 rainfall record, as processed by Model 1, with the interannual variations in vertical displacement
 991 recorded at the GNSS Rite Station (Fig. 8d₁). Each of the produced 1000 synthetic daily rain amount
 992 records are processed by Model 1 to produce 1000 synthetic interannual water accumulation
 993 fluctuations equivalent to those shown by the blue curve in Fig. 8c₁. We evaluate the Pearson linear
 994 correlation coefficients, R_i ($i = 1, \dots, 1000$), between these 1000 synthetic records with the interannual
 995 variations in vertical displacement recorded at the GNSS Rite Station (Fig. 8d₁) from 01/01/1987 to
 996 12/30/2024. We found that 81% of the 1000 synthetic records produced R values lower than R_o , which
 997 is the correlation coefficient found above in point 1. Moreover, we calculate the standard deviation,
 998 A_i ($i = 1, \dots, 1000$), of these 1000 synthetic records from 01/01/1987 to 12/30/2024 as estimates the
 999 amplitude of the produced fluctuations. We calculate the standard deviation of the real interannual
 1000 water accumulation fluctuation record to be $A_o = 42$ cm. We found that the distribution of the 1000
 1001 A_i ($i = 1, \dots, 1000$), of the synthetic records has an average $\mu = 26$ cm and a standard deviation $\sigma = 5$ cm.
 1002 This means that the real $A_o = 42$ cm is outside the typical three-sigma range of the synthetic
 1003 ensemble which covers around 99.7% of the total probability; therefore, from a statistical point of
 1004 view the ensemble of the 1000 synthetic water accumulation records is not statistically compatible
 1005 with the actual one.

10063. If instead of the rain record, it is shuffled the interannual variations in vertical displacement recorded
 1007 at the GNSS Rite Station (Fig. 8d₁), we found that 100% of the 1000 synthetic records produced R
 1008 values lower than R_o .

1009

1010 The above tests suggest that the interannual water accumulation fluctuation record obtained with
 1011 actual data shows dynamical patterns much more pronounced than those obtained with the synthetic
 1012 ones, and these patterns appear to be sufficiently well correlated with the interannual variations in
 1013 vertical displacement recorded at the GNSS Rite Station (Fig. 8d₁) as suggested by the statistical test
 1014 in point 1.

1015

1016 **CRediT authorship contribution statement**1017 **Scafetta N.**: Writing – review & editing, Writing – original draft, Software, Methodology, Investigation,
1018 Geophysical Data curation, Formal analysis.1019 **Lima A.**: Writing – review & editing, Writing – original draft, Investigation, Supervision.1020 **Milia A.**: Writing – review & editing, Writing – original draft, Investigation, Geological Data curation.1021 **Spera F.**: Writing – review & editing.1022 **Bodnar RJ**: Writing – review & editing.1023 **De Vivo B**: Writing – review & editing.1024 **Daniele L**: Writing – review & editing.

1025

1026 **Declaration of competing interest**1027 The authors declare that they have no known competing financial interests or personal relationships
1028 that could have appeared to influence the work reported in this paper. Co-author Nicola Scafetta is
1029 an Associate Editor of this Journal and was not involved in the editorial review or the decision to
1030 publish this article.

1031

Journal Pre-proofs

1033 **References**

1034

1035 1036 AGIP, 1987. Geologia e geofisica del sistema geotermico dei Campi Flegrei. Internal report, AGIP S.p.A., Milan, Italy (in Italian).

1037 1038 1039 Aiuppa, A., Federico, C., Giudice, G., Gurrieri, S., Liuzzo, M., Shinohara, H., Favara, R., Valenza, M., 2006. Rates of carbon dioxide plume degassing from Mount Etna volcano. *J. Geophys. Res. Solid Earth* 111, B09207. <https://doi.org/10.1029/2006JB004307>

1040 1041 Bear, J., 1972. Dynamics of Fluids in Porous Media. Elsevier, New York. (Reprinted by Dover Publications, 1988).

1042 1043 1044 Becken, M., Ritter, O., Bedrosian, P.A., Weckmann, U., 2011. Correlation between deep fluids, tremor and creep along the central San Andreas fault. *Nature* 480(7375), 87–90. <https://doi.org/10.1038/nature10609>

1045 1046 1047 Belkin, H.E., De Vivo, B., 2023. Compositional variation and zoning of epidote supergroup minerals in the Campi Flegrei geothermal field, Naples, Italy. *Eur. J. Mineral.* 35, 25–44. <https://doi.org/10.5194/ejm-35-25-2023>

1048 1049 1050 Belkin, H.E., McAleer, R.J., De Vivo, B., Croke, M.R., 2023. Mofete and San Vito geothermal field ore mineralization data [dataset]. U.S. Geological Survey Data Release. <https://doi.org/10.5066/P9HNDG4F>

1051 1052 1053 Belkin, H.E., McAleer, R.J., De Vivo, B., 2024. Ore mineralization in the Mofete and San Vito geothermal fields, Campi Flegrei volcanic complex, Naples, Italy. *J. Geochem. Explor.* 264, 107556. <https://doi.org/10.1016/j.gexplo.2024.107556>

1054 1055 1056 Bernard, P., Zollo, A., 1989. The Irpinia (Italy) 1980 earthquake: Detailed analysis of a complex normal faulting. *J. Geophys. Res. Solid Earth* 94(B2), 1631–1647. <https://doi.org/10.1029/JB094iB02p01631>

1057 1058 1059 Bernasconi, A., Bruni, P., Gorla, L., Principe, C., Sbrana, A., 1981. Risultati preliminari dell'esplorazione geotermica profonda nell'area vulcanica del Somma–Vesuvio. *Rend. Soc. Geol. Ital.* 4, 237–240.

1060 1061 1062 Bevilacqua, A., Neri, A., De Martino, P., Giudicepietro, F., Macedonio, G., Ricciolino, P., 2024. Simulation of eruption scenarios and hazard quantification at Campi Flegrei caldera. *Commun. Earth Environ.* 5, 742. <https://doi.org/10.1038/s43247-024-01865-y>

1063 1064 1065 Bodnar, R.J., Cannatelli, C., De Vivo, B., Lima, A., Belkin, H.E., Milia, A., 2007. Quantitative model for magma degassing and ground deformation (bradyseism) at Campi Flegrei, Italy: Implications for future eruptions. *Geology* 35(9), 791–794. <https://doi.org/10.1130/G23653A.1>

1066 1067 Bonafede, M., Mazzanti, M., 1997. Hot fluid migration in compressible saturated porous media. *Geophys. J. Int.* 128, 383–398. <https://doi.org/10.1111/j.1365-246X.1997.tb01562.x>

1068 1069 1070 Brocchini, D., Principe, C., Castradori, D., Laurenzi, M.A., Gorla, L., 2001. Quaternary evolution of the southern sector of the Campanian Plain and early Somma–Vesuvius activity: Insights from the Trecase 1 well. *Mineral. Petrol.* 73(1–2), 67–91. <https://doi.org/10.1007/s007100170011>

1071 Bruno, P.G., Ricciardi, G.P., Petrillo, Z., Di Fiore, V., Troiano, A., Chiodini, G., 2007. Geophysical
 1072 and hydrogeological experiments from a shallow hydrothermal system at Solfatara Volcano,
 1073 Campi Flegrei, Italy: Response to caldera unrest. *J. Geophys. Res. Solid Earth* 112, B06201.
 1074 <https://doi.org/10.1029/2006JB004383>

1075 Burnham, C.W., 1979. Magmas and hydrothermal fluids. In: Barnes, H.L. (Ed.), *Geochemistry of*
 1076 *Hydrothermal Ore Deposits*. Wiley, New York, pp. 71–136.

1077 Caliro, S., Avino, R., Capecchiacci, F., Carandente, A., Chiodini, G., Cuoco, E., Minopoli, C.,
 1078 Rufino, F., Santi, A., Rizzo, A.L., Aiuppa, A., Allocca, V., De Vita, P., Di Vito, M.A., 2025.
 1079 Chemical and isotopic characterization of groundwater and thermal waters from the Campi
 1080 Flegrei caldera (southern Italy). *J. Volcanol. Geotherm. Res.* 460, 108280.
 1081 <https://doi.org/10.1016/j.jvolgeores.2025.108280>

1082 Cannatelli, C., Spera, F.J., Bodnar, R.J., Lima, A., De Vivo, B., 2020. Ground movement
 1083 (bradyseism) in the Campi Flegrei volcanic area: A review. In: De Vivo, B., Belkin, H.E.,
 1084 Rolandi, G. (Eds.), *Vesuvius, Campi Flegrei, and Campanian Volcanism*. Elsevier, Amsterdam,
 1085 pp. 407–433.

1086 Caprarelli, G., Tsutsumi, M., Turi, B., 1997. Chemical and isotopic signatures of the basement rocks
 1087 from the Campi Flegrei geothermal field (Naples, southern Italy): Inferences about the origin
 1088 and evolution of its hydrothermal fluids. *J. Volcanol. Geotherm. Res.* 76, 63–82.
 1089 [https://doi.org/10.1016/S0377-0273\(96\)00072-8](https://doi.org/10.1016/S0377-0273(96)00072-8)

1090 Carella, R., Guglielminetti, M., 1983. Buffers in the Mofete Field, Naples, Italy. In: *Proceedings of*
 1091 *the 9th Workshop on Geothermal Reservoir Engineering*, Stanford University, Stanford, CA.

1092 Carlino, S., 2021. Brief history of volcanic risk in the Neapolitan area (Campania, Southern Italy): A
 1093 critical review. *Nat. Hazards Earth Syst. Sci.* 21, 3097–3112. <https://doi.org/10.5194/nhess-21-3097-2021>.

1095 Casertano, L., Oliveri del Castillo, A., Quagliariello, M.T., 1976. Hydrodynamics and geodynamics
 1096 in the Phleorean Fields area of Italy. *Nature* 264, 154–161. <https://doi.org/10.1038/264161a0>

1097 Cerrone, C., Ascione, A., Robustelli, G., Tuccimei, P., Soligo, M., Balassone, G., Mormone, A.,
 1098 2021. Late Quaternary uplift and sea level fluctuations along the Tyrrhenian margin of
 1099 Basilicata–northern Calabria (southern Italy): New constraints from raised paleoshorelines.
 1100 *Geomorphology* 395, 107978. <https://doi.org/10.1016/j.geomorph.2021.107978>

1101 Chiodini, G., Giudicepietro, F., Vandemeulebrouck, J., Aiuppa, A., Caliro, S., De Cesare, W.,
 1102 Tamburello, G., Avino, R., Orazi, M., D'Auria, L., 2017. Fumarolic tremor and geochemical
 1103 signals during a volcanic unrest. *Geology* 45(12), 1131–1134. <https://doi.org/10.1130/G39447.1>

1104 Cipriani, A., Marianelli, P., Sbrana, A., 2008. Studio di una sequenza piroclastica del vulcano della
 1105 Solfatara (Campi Flegrei). Considerazioni vulcanologiche e sul sistema di alimentazione. *Boll.*
 1106 *Soc. Tosc. Sci. Nat. Ser. A* 113, 39–48.

1107 De Landro, G., Vanorio, T., Muzellec, T., Russo, G., Lomax, A., Virieux, J., Zollo, A., 2025. 3D
 1108 structure and dynamics of Campi Flegrei enhance multi-hazard assessment. *Nat. Commun.* 16,
 1109 59821. <https://doi.org/10.1038/s41467-025-59821-z>

1110 Del Gaudio, C., Aquino, I., Ricciardi, G.P., Ricco, C., Scandone, R., 2010. Unrest episodes at Campi
 1111 Flegrei: A reconstruction of vertical ground movements during 1905–2009. *J. Volcanol.*
 1112 *Geotherm. Res.* 195(1), 48–56. <https://doi.org/10.1016/j.jvolgeores.2010.05.014>

1113 De Siena, L., Chiodini, G., Vilardo, G., Del Pezzo, E., Castellano, M., Colombelli, S., Tisato, N.,
 1114 Ventura, G., 2017. Source and dynamics of a volcanic caldera unrest: Campi Flegrei, 1983–84.
 1115 *Sci. Rep.* 7, 8099. <https://doi.org/10.1038/s41598-017-08192-7>

1116 Detournay, E., Cheng, A.H.D., 1993. Fundamentals of poroelasticity. In: Fairhurst, C. (Ed.),
 1117 *Comprehensive Rock Engineering: Principles, Practice and Projects*, Vol. II. Pergamon Press,
 1118 Oxford, pp. 113–171.

1119 De Vivo, B., Belkin, H.E., Barbieri, M., Chelini, W., Lattanzi, P., Lima, A., Tolomeo, L., 1989. The
 1120 Campi Flegrei (Italy) geothermal system: A fluid inclusion study of the Mofete and San Vito
 1121 fields. *J. Volcanol. Geotherm. Res.* 36(4), 303–326. [https://doi.org/10.1016/0377-0273\(89\)90076-0](https://doi.org/10.1016/0377-0273(89)90076-0)

1123 De Vivo, B., Rolandi, G., Gans, P.B., Calvert, A., Bohrson, W.A., Spera, F.J., Belkin, H.E., 2001.
 1124 New constraints on the pyroclastic eruptive history of the Campanian volcanic Plain (Italy).
 1125 *Mineral. Petrol.* 73, 47–65. <https://doi.org/10.1007/s007100170010>

1126 De Vivo, B., Lima, A., 2006. A hydrothermal model for ground movements (bradyseism) at Campi
 1127 Flegrei, Italy. In: De Vivo, B. (Ed.), *Volcanism in the Campania Plain: Vesuvius, Campi Flegrei*
 1128 and Ignimbrites. *Dev. Volcanol.* 9. Elsevier, Amsterdam, pp. 289–317.

1129 De Vivo, B., Lima, A., Bodnar, R.J., Milia, A., Spera, F.J., 2009. Il rischio di eruzione nei Campi
 1130 Flegrei. *Le Scienze* 496, 96–103 (in Italian)

1131 De Vivo, B., Rolandi, G., 2020. Volcanological risk associated with Vesuvius and Campi Flegrei. In:
 1132 De Vivo, B., Belkin, H.E., Rolandi, G. (Eds.), *Vesuvius, Campi Flegrei, and Campanian*
 1133 *Volcanism*. Elsevier, Amsterdam, pp. 471–492.

1134 Evans, M.A., Fisher, M.P., 2012. On the distribution of fluids in folds: A review of controlling factors
 1135 and processes. *J. Struct. Geol.* 44, 2–24. <https://doi.org/10.1016/j.jsg.2012.08.003>

1136 Farquharson, J.I., Amelung, F., 2020. Extreme rainfall triggered the 2018 rift eruption at Kīlauea
 1137 Volcano. *Nature* 580, 491–495. <https://doi.org/10.1038/s41586-020-2172-5>

1138 Fortelli, A., Scafetta, N., Mazzarella, A., 2019. Nowcasting and real-time monitoring of heavy rainfall
 1139 events inducing flash-floods: An application to Phlegraean area (Central-Southern Italy). *Nat.*
 1140 *Hazards* 97, 861–889. <https://doi.org/10.1007/s11069-019-03680-7>

1141 Freeze, R.A., Cherry, J.A., 1979. *Groundwater*. Prentice-Hall Inc., Englewood Cliffs, NJ.

1142 Glazner, A.F., McNutt, S.R., 2021. Relationship between dike injection and b-value for volcanic
 1143 earthquake swarms. *J. Geophys. Res. Solid Earth* 126, e2020JB021631.
 1144 <https://doi.org/10.1029/2020JB021631>

1145 Guerriero, V., Mazzoli, S., 2021. Theory of effective stress in soil and rock and implications for
 1146 fracturing processes: A review. *Geosciences* 11(3), 119.
 1147 <https://doi.org/10.3390/geosciences11030119>

1148 Hainzl, S., Kraft, T., Wassermann, J., Igel, H., Schmedes, E., 2006. Evidence for rainfall-triggered
 1149 earthquake activity. *Geophys. Res. Lett.* 33(19), L19303.
 1150 <https://doi.org/10.1029/2006GL027642>

1151 Hersbach, H., Bell, B., Berrisford, P., 2020. The ERA5 global reanalysis. *Q. J. R. Meteorol. Soc.*
 1152 146(730), 1999–2049. <https://doi.org/10.1002/qj.3803>

1153 Husen, S., Bachmann, C., Giardini, D., 2007. Locally triggered seismicity in the central Swiss Alps
 1154 following the large rainfall event of August 2005. *Geophys. J. Int.* 171(3), 1126–
 1155 1134. <https://doi.org/10.1111/j.1365-246X.2007.03561.x>

1156 Isaia, R., Troiano, A., Di Giuseppe, M.G., De Paola, C., Gottsmann, J., Pagliara, F., Smith, V.C.,
 1157 Stock, M.J., 2025. 3D magnetotelluric imaging of a transcrustal magma system beneath the
 1158 Campi Flegrei caldera, southern Italy. *Commun. Earth Environ.* 6, 213.
 1159 <https://doi.org/10.1038/s43247-025-02185-5>

1160 Jiménez, M.J., García-Fernández, M., 2000. Occurrence of shallow earthquakes following periods of
 1161 intense rainfall in Tenerife, Canary Islands. *J. Volcanol. Geotherm. Res.* 103(1–4), 463–468.
 1162 [https://doi.org/10.1016/S0377-0273\(00\)00237-7](https://doi.org/10.1016/S0377-0273(00)00237-7)

1163 Judenherc, S., Zollo, A., 2004. The bay of Naples (Southern Italy): Constraints on the volcanic
 1164 structures inferred from a dense seismic survey. *J. Geophys. Res. Solid Earth* 109, B10312.
 1165 <https://doi.org/10.1029/2003JB002876>

1166 Kraft, T., Wassermann, J., Schmedes, E., Igel, H., 2006. Meteorological triggering of earthquake
 1167 swarms at Mt. Hochstaufen, SE-Germany. *Tectonophysics* 424(3–4), 245–
 1168 258. <https://doi.org/10.1016/j.tecto.2006.03.044>

1169 Lima, A., De Vivo, B., Spera, F.J., Bodnar, R.J., Milia, A., Nunziata, C., Belkin, H.E., Cannatelli, C.,
 1170 2009. Thermodynamic model for the uplift and deflation episodes (bradyseism) associated with
 1171 magmatic–hydrothermal activity at the Campi Flegrei active volcanic center (Italy). *Earth-Sci.
 1172 Rev.* 97, 44–58. <https://doi.org/10.1016/j.earscirev.2009.10.001>

1173 Lima, A., Bodnar, R.J., De Vivo, B., Spera, F.J., Belkin, H.E., 2021. Interpretation of recent unrest
 1174 events (bradyseism) at Campi Flegrei, Napoli (Italy): Comparison of models based on cyclical
 1175 hydrothermal events versus shallow magmatic intrusive events. *Geofluids* 2021,
 1176 2000255. <https://doi.org/10.1155/2021/2000255>

1177 Lima, A., Bodnar, R.J., De Vivo, B., Spera, F.J., Belkin, H.E., 2025a. The “breathing” Earth (la terra
 1178 che respira) at Solfatara–Pisciarelli (Campi Flegrei, southern Italy) during 2005–2024: Nature’s
 1179 way of attenuating the effects of bradyseism through gradual and episodic release of subsurface
 1180 pressure. *Am. Mineral.* 110, 820–825. <https://doi.org/10.2138/am-2024-9516>

1181 Lima, A., Macedonio, G., Esposito, R., Belkin, H.E., 2025b. Magma–carbonate country rock
 1182 interaction can provide H₂O during magma ascent: Results from fluid and melt inclusions in
 1183 skarn xenoliths from Breccia Museo, Campi Flegrei (Southern Italy). *J. Volcanol. Geotherm.
 1184 Res.* 466, 108405. <https://doi.org/10.1016/j.jvolgeores.2025.108405>

1185 Mantiloni, L., Hickey, J., Alshembari, R., 2025. The role of gravity in the state of stress and pore
 1186 pressure of poroelastic rocks. *Geophys. J. Int.* 242(1), ggaf169.
 1187 <https://doi.org/10.1093/gji/ggaf169>

1188 Marini, L., Principe, C., Lelli, M., 2022. The Solfatara Magmatic–Hydrothermal System:
 1189 Geochemistry, Geothermometry and Geobarometry of Fumarolic Fluids. *Advances in*
 1190 *Volcanology*. Springer, Cham, 375 pp. <https://doi.org/10.1007/978-3-030-98471-7>

1191 Marini, L., Principe, C., Lelli, M., 2025. Time changes during the last 40 years in the Solfatara
 1192 magmatic–hydrothermal system (Campi Flegrei, Italy): New conceptual model and future
 1193 scenarios. *Solid Earth* 16, 551–578. <https://doi.org/10.5194/se-16-551-2025>

1194 Mastin, L.G., 1993. Can Rain Cause Volcanic Eruptions? U.S. Geological Survey Open-File Report,
 1195 pp. 93–445.

1196 Mazzarella, A., Palumbo, A., 1989. Does the solar cycle modulate seismic and volcanic activity? *J.*
 1197 *Volcanol. Geotherm. Res.* 39, 89–93. [https://doi.org/10.1016/0377-0273\(89\)90023-1](https://doi.org/10.1016/0377-0273(89)90023-1)

1198 Milia, A., Torrente, M.M., 1997. Evoluzione tettonica della Penisola Sorrentina (margine
 1199 peritirrenico campano). *Boll. Soc. Geol. Ital.* 116, 487–502.

1200 Milia, A., Torrente, M.M., 1999. Tectonics and stratigraphic architecture of a peri-Tyrrhenian half-
 1201 graben (Bay of Naples, Italy). *Tectonophysics* 315, 301–318. [https://doi.org/10.1016/S0040-1951\(99\)00280-2](https://doi.org/10.1016/S0040-1951(99)00280-2)

1203 Milia, A., 2000. The Dohrn Canyon formation: A response to the eustatic fall and tectonic uplift of
 1204 the outer shelf (Eastern Tyrrhenian Sea margin, Italy). *Geo-Mar. Lett.* 20, 101–108.

1205 Milia, A., Torrente, M.M., 2000. Fold uplift and synkinematic stratal architectures in a region of
 1206 active transtensional tectonics and volcanism, eastern Tyrrhenian Sea. *Geol. Soc. Am. Bull.*
 1207 112(10), 1531–1542. [https://doi.org/10.1130/0016-7606\(2000\)112<1531:FUASSA>2.0.CO;2](https://doi.org/10.1130/0016-7606(2000)112<1531:FUASSA>2.0.CO;2)

1208 Milia, A., Torrente, M.M., Giordano, F., 2000. Active deformation and volcanism offshore Campi
 1209 Flegrei, Italy: New data from high-resolution seismic reflection profiles. *Mar. Geol.* 171(1–4),
 1210 61–73. [https://doi.org/10.1016/S0025-3227\(00\)00111-0](https://doi.org/10.1016/S0025-3227(00)00111-0)

1211 Milia, A., Giordano, F., 2002. Holocene stratigraphy and depositional architecture of eastern Pozzuoli
 1212 Bay (eastern Tyrrhenian Sea margin, Italy): The influence of tectonics and wave-induced
 1213 currents. *Geo-Mar. Lett.* 22, 42–50. <https://doi.org/10.1007/s00367-002-0095-9>

1214 Milia, A., Torrente, M.M., 2003. Late Quaternary volcanism and transtensional tectonics in the Bay
 1215 of Naples, Campania continental margin, Italy. *Mineral. Petrol.* 79(1–2), 49–65.

1216 Milia, A., Torrente, M.M., Russo, M., Zuppetta, A., 2003. Tectonics and crustal structure of the
 1217 Campania continental margin: Relationships with volcanism. *Mineral. Petrol.* 79, 33–47.
 1218 <https://doi.org/10.1007/s00710-003-0005-5>

1219 Milia, A., Torrente, M.M., Giordano, F., Mirabile, L., 2006. Rapid changes of the accommodation
 1220 space in the Late Quaternary succession of Naples Bay, Italy: The influence of volcanism and
 1221 tectonics. In: De Vivo, B. (Ed.), *Volcanism of the Campania Plain*. Dev. Volcanol. 9. Elsevier,
 1222 Amsterdam, pp. 53–68.

1223 Milia, A., Torrente, M.M., 2011. The possible role of extensional faults in localizing magmatic
 1224 activity: A crustal model for the Campanian Volcanic Zone (eastern Tyrrhenian Sea, Italy). *J.*
 1225 *Geol. Soc.* 168, 471–484. <https://doi.org/10.1144/0016-76492010-121>

1226 Milia, A., Torrente, M.M., 2015a. Tectono-stratigraphic signature of a rapid multistage subsiding rift
 1227 basin in the Tyrrhenian–Apennine hinge zone (Italy): A possible interaction of upper plate with
 1228 subducting slab. *J. Geodyn.* 86, 42–60. <https://doi.org/10.1016/j.jog.2015.02.005>

1229 Milia, A., Torrente, M.M., 2015b. Rift and supradetachment basins during extension: Insight from
 1230 the Tyrrhenian rift. *J. Geol. Soc.* 172(1), 5–8. <https://doi.org/10.1144/jgs2014-046>

1231 Milia, A., Torrente, M.M., 2020. Space–time evolution of an active volcanic field in an extensional
 1232 region: The example of the Campania margin (eastern Tyrrhenian Sea). In: De Vivo, B., Belkin,
 1233 H.E., Rolandi, G. (Eds.), *Vesuvius, Campi Flegrei, and Campanian Volcanism*. Elsevier,
 1234 Amsterdam, pp. 297–321.

1235 Montgomery-Brown, E.K., Shelly, D.R., Hsieh, P.A., 2019. Snowmelt-triggered earthquake swarms
 1236 at the margin of Long Valley Caldera, California. *Geophys. Res. Lett.* 46(7), 3698–3705.
 1237 <https://doi.org/10.1029/2019GL082254>

1238 Morgan, D.J., Blake, S., Rogers, N.W., De Vivo, B., Rolandi, G., Davidson, J.P., 2006. Magma
 1239 chamber recharge at Vesuvius in the century prior to the eruption of A.D. 79. *Geology* 34(10),
 1240 845–848. <https://doi.org/10.1130/G22604.1>

1241 Natale, J., Vitale, S., Isaia, R., 2024. Simultaneous normal and reverse faulting in reactivating caldera
 1242 faults: A detailed field structural analysis from Campi Flegrei (southern Italy). *J. Struct. Geol.*
 1243 181, 105109. <https://doi.org/10.1016/j.jsg.2024.105109>

1244 Orsi, G., 2022. Volcanic and deformation history of the Campi Flegrei volcanic field, Italy. In: Orsi,
 1245 G., D’Antonio, M., Civetta, L. (Eds.), *Campi Flegrei: A Restless Caldera in a Densely Populated*
 1246 *Area*. Springer, Cham, pp. 1–53. <https://doi.org/10.1007/978-3-642-37060-1>

1247 Orsi, G., Di Vito, M., Selva, J., Marzocchi, W., 2009. Long-term forecast of eruption style and size
 1248 at Campi Flegrei caldera (Italy). *Earth Planet. Sci. Lett.* 287(1–2), 265–276.
 1249 <https://doi.org/10.1016/j.epsl.2009.08.013>

1250 Palumbo, A., 1985. Influence of external tidal and meteorological forces on the bradyseismic
 1251 phenomenon in the Phlegraean Fields. *IL Nuovo Cimento C* 8(5), 538–551.

1252 Petrillo, Z., Chiodini, G., Mangiacapra, A., Caliro, S., Capuano, P., Russo, G., Cardellini, C., Avino,
 1253 R., 2013. Defining a 3D physical model for the hydrothermal circulation at Campi Flegrei
 1254 caldera (Italy). *J. Volcanol. Geotherm. Res.* 264, 172–182.
 1255 <https://doi.org/10.1016/j.jvolgeores.2013.08.008>

1256 Petrosino, S., Cusano, P., Madonia, P., 2018. Tidal and hydrological periodicities of seismicity reveal
 1257 new risk scenarios at Phlegraean Area caldera. *Sci. Rep.* 8, 13808.
 1258 <https://doi.org/10.1038/s41598-018-31760-4>

1259 Ramsay, J.G., 1967. *Folding and Fracturing of Rocks*. McGraw-Hill, New York, 568 pp.

1260 Rolandi, G., Bellucci, F., Heizler, M.T., Belkin, H.E., De Vivo, B., 2003. Tectonic controls on the
 1261 genesis of ignimbrites from the Campanian Volcanic Zone, Southern Italy. *Mineral. Petrol.* 79,
 1262 3–31. <https://doi.org/10.1007/s00710-003-0014-4>

1263 Rolandi, G., Troise, C., Sacchi, M., Di Lascio, M., De Natale, G., 2025. The 1538 eruption at the
 1264 Campi Flegrei resurgent caldera: Implications for future unrest and eruptive scenarios. *Nat.*
 1265 *Hazards Earth Syst. Sci.* 25, 3421–3453. <https://doi.org/10.5194/nhess-25-3421-2025>

1266 Rosi, M., Sbrana, A., 1987. The Phleorean Fields. Quaderni de "La Ricerca Scientifica", CNR, 175
1267 pp.

1268 Roth, P., Pavoni, N., Deichmann, N., 1992. Seismotectonics of the eastern Swiss Alps and evidence
1269 for precipitation-induced variations of seismic activity. *Tectonophysics* 207(1–2), 183–197.
1270 [https://doi.org/10.1016/0040-1951\(92\)90477-N](https://doi.org/10.1016/0040-1951(92)90477-N)

1271 Saar, M.O., Manga, M., 2003. Seismicity induced by seasonal groundwater recharge at Mt. Hood,
1272 Oregon. *Earth Planet. Sci. Lett.* 214(3–4), 605–618. [https://doi.org/10.1016/S0012-821X\(03\)00418-7](https://doi.org/10.1016/S0012-821X(03)00418-7)

1274 Scafetta, N., Grigolini, P., Imholt, T., Roberts, J., West, B.J., 2004. Solar turbulence in Earth's global
1275 and regional temperature anomalies. *Phys. Rev. E* 69, 026303.
1276 <https://doi.org/10.1103/PhysRevE.69.026303>

1277 Scafetta, N., Mazzarella, A., 2021. On the rainfall triggering of Phlegraean Fields volcanic tremors.
1278 *Water* 13(2), 154. <https://doi.org/10.3390/w13020154>

1279 Scuderi, M., Collettini, C., 2016. The role of fluid pressure in induced vs. triggered seismicity:
1280 Insights from rock deformation experiments on carbonates. *Sci. Rep.* 6, 24852.
1281 <https://doi.org/10.1038/srep24852>

1282 Sibson, R.H., 1996. Structural permeability of fluid-driven fault-fracture meshes. *J. Struct. Geol.*
1283 18(8), 1031–1042. [https://doi.org/10.1016/0191-8141\(96\)00032-6](https://doi.org/10.1016/0191-8141(96)00032-6)

1284 Sibson, R.H., 2003. Brittle-failure controls on maximum sustainable overpressure in different
1285 tectonic regimes. *AAPG Bull.* 87(6), 901–908.

1286 Siniscalchi, A., Tripaldi, S., Romano, G., Chiodini, G., Impronta, L., Petrillo, Z., D'Auria, L., Caliro,
1287 S., Avino, R., 2019. Reservoir structure and hydraulic properties of the Campi Flegrei
1288 geothermal system inferred by audiomagnetotelluric, geochemical, and seismicity study. *J.*
1289 *Geophys. Res. Solid Earth* 124(5), 5336–5356. <https://doi.org/10.1029/2018JB016514>

1290 Tan, X., Tramelli, A., Gammaldi, S., Beroza, G.C., Ellsworth, W.L., Marzocchi, W., 2025. A clearer
1291 view of the current phase of unrest at Campi Flegrei Caldera. *Science* 390(6768), 70–75.
1292 <https://doi.org/10.1126/science.adw9038>

1293 Todesco, M., 2021. Caldera's breathing: Poroelastic ground deformation at Campi Flegrei (Italy).
1294 *Front. Earth Sci.* 9, 702665. <https://doi.org/10.3389/feart.2021.702665>

1295 Torrente, M.M., Milia, A., 2013. Volcanism and faulting of the Campania margin (Eastern
1296 Tyrrhenian Sea, Italy): A three-dimensional visualization of a new volcanic field off Campi
1297 Flegrei. *Bull. Volcanol.* 75, 719. <https://doi.org/10.1007/s00445-013-0719-0>

1298 Tramelli, A., Convertito, V., Godano, C., 2024. b value enlightens different rheological behaviour in
1299 Campi Flegrei caldera. *Commun. Earth Environ.* 5, 275. <https://doi.org/10.1038/s43247-024-01447-y>

1301 Tramelli, A., Giudicepietro, F., Ricciolino, P., Chiodini, G., 2022. The seismicity of Campi Flegrei
1302 in the context of an evolving long-term unrest. *Sci. Rep.* 12, 2900.
1303 <https://doi.org/10.1038/s41598-022-06928-8>

1304 Ueda, T., Kato, A., 2019. Seasonal variations in crustal seismicity in San-in District, Southwest Japan.
1305 *Geophys. Res. Lett.* 46(6), 3172–3179. <https://doi.org/10.1029/2018GL081789>

1306 Vanorio, T., Geremia, D., De Landro, G., Guo, T., 2025. The recurrence of geophysical
1307 manifestations at the Campi Flegrei caldera. *Sci. Adv.* 11(18), ead^t2067.
1308 <https://doi.org/10.1126/sciadv.adt2067>

1309 Wang, C., Manga, M., 2021. Water and Earthquakes. Springer, Cham, 387 pp.
1310 <https://doi.org/10.1007/978-3-030-64308-9>

1311 Warren, N.W., Latham, G.V., 1970. An experimental study of thermally induced microfracturing and
1312 its relation to volcanic seismicity. *J. Geophys. Res.* 75(23), 4455–4464.
1313 <https://doi.org/10.1029/JB075i023p04455>

1314 Wiemer, S., McNutt, S.R., 1997. Variations in the frequency–magnitude distribution with depth in
1315 two volcanic areas: Mount St. Helens, Washington, and Mt. Spurr, Alaska. *Geophys. Res. Lett.*
1316 24, 189–192. <https://doi.org/10.1029/96GL03779>

1317 Wyss, M., 1973. Towards a physical understanding of the earthquake frequency distribution.
1318 *Geophys. J. Int.* 31, 341–359. <https://doi.org/10.1111/j.1365-246X.1973.tb06506.x>

1319 Zollo, A., Maercklin, N., Vassallo, M., Iacono, D.D., Virieux, J., Gasparini, P., 2008. Seismic
1320 reflections reveal a massive melt layer feeding Campi Flegrei caldera. *Geophys. Res. Lett.* 35,
1321 L12306. <https://doi.org/10.1029/2008GL034242>

1322

1323

Figure captions

1324

1325 **Figure 1.** (a) Structural map of the Vavilov Basin-Eastern Tyrrhenian Margin; the green faults are
 1326 Pliocene in age in the Central Tyrrhenian Sea and Lower Pleistocene in the Eastern Tyrrhenian
 1327 Margin, the orange faults are Middle Pleistocene, the white faults are late Quaternary in age. CA:
 1328 Cancello borehole; TC: Trecase borehole. Modified from Milia et al. (2015, 2017). (b) Structural map
 1329 of the Campanian Margin from the Sorrento Peninsula to the Campi Flegrei area. White faults are
 1330 Middle Pleistocene in age; Red faults are Late Quaternary in age (PP: Penta Palummo; MB: Miseno
 1331 Bank; DB: Monte Dolce dike; NC: Nisida Complex). Modified from Milia and Torrente (2011). (c)
 1332 NW-SE geologic section across the Campanian Margin that shows the stratigraphy of the Naples
 1333 Bay-Campi Flegrei half-graben bounded by the Middle Pleistocene-late Quaternary NE-SW trending
 1334 normal faults (Modified from Milia et al., 2003; Milia and Torrente, 2011, 2020).

1335

1336 **Figure 2.** (a) Structural map of the Campi Flegrei–Pozzuoli Bay area (from Milia and Torrente,
 1337 2000): 1. Onshore; 2. Offshore, highly fractured areas (affected by an uplift of 100%–50%); 3.
 1338 Normal faults; 4. Crest of the Pozzuoli anticline; 5. Trough of the Pozzuoli syncline. Black stars
 1339 indicate the location of deep geothermal boreholes (Mofete - MF1, MF2, MF5, and San Vito - SV1,
 1340 SV3). (b) Google Earth CF map showing the hypothesized three concentric buffers used in the model
 1341 (R1-R2-R3) into which the CF region is conceptually divided considering the tectonic areas (red fault
 1342 lines) shown in (a), which are interpreted to be characterized by different hydraulic conductivities.
 1343 (c) Seismic section across the Syncline (Epitaffio Valley) offshore Pozzuoli along line C shown on
 1344 Fig. 2a (modified from Milia et al., 2000). (d) Seismic section through the faulted zone offshore
 1345 Pozzuoli along line D shown on Fig. 2a (modified from Milia et al., 2000).

1346

1347 **Figure 3.** Ground displacement at Pozzuoli Porto since 1905, measured by precision leveling (until
 1348 year 2000, in red) and using data from the nearby GPS benchmark of Rione Terra (since 2000, blue
 1349 dots) (from the Bulletins of the Osservatorio Vesuviano, INGV and Bevilacqua et al., 2024). (Inset)
 1350 Reconstruction of the vertical displacement of the Serapeo fourth floor in Pozzuoli, from the 3rd
 1351 century AD to the present (Rolandi et al., 2025).

1352

1353 **Figure 4.** Schematic migration pathways for both meteoric and deep magmatic fluids. Fluids in the
 1354 reservoir Unit C are confined by the Unit D that thins out and disappears beneath the Gulf of Pozzuoli,
 1355 where fluids can migrate up to the seafloor surface to produce the observed pockmarks. E-W oriented
 1356 geologic section across the Solfatara-Pozzuoli area and Pozzuoli Bay (for location see Fig. 1a). The
 1357 various geologic and stratigraphic features shown include faults and fractures in red. Colour legend:
 1358 (1) Magma depth (Zollo et al., 2008); (2) Crystallized magma (Lima et al., 2025a and references
 1359 therein); (3) Crystalline/carbonate lithologies; (4) Unit A (1.0–0.7 Ma), made up of continental to
 1360 shallow marine deposits, representing the deeper reservoir of magmatic fluids (Milia and Torrente,
 1361 2015a, 2015b; Lima et al., 2025a and references therein); (5) Unit B (0.7–0.4 Ma), mainly made up
 1362 of clays representing the deeper impermeable unit; (6) Unit C (0.4–0.1 Ma), made up of silts and
 1363 sands with localized old lava lenses, representing the shallow reservoir containing mostly meteoric
 1364 and sea waters; (7) Pyroclastic deposits including the Campanian Ignimbrite deposits (Unit D, < 0.1
 1365 Ma) representing a relatively impermeable unit compared to overlying and underlying units, this Unit
 1366 D is highly permeable where highly fractured and faulted; (8) Yellow Tuff deposits (<35 ka); (9)

1367 Marine clastic sediments (silts and sands) in Pozzuoli Bay, the unconformity marks the boundary
1368 between the pre-folding strata and syn-folding deposits; (10) Alluvial deposits onshore.

1369

1370

Journal Pre-proofs

1371 Figure 5. N-S oriented seismic sections supporting the interpretation of fluid pathway in the
 1372 stratigraphic succession offshore Campi Flegrei. (a) Map showing the distribution of the Campanian
 1373 Ignimbrite and location of the seismic profiles shown in (b) and (c). (b) Multichannel seismic section
 1374 showing Unit A characterized by parallel reflectors (1) that transitions to a high amplitude scattered
 1375 reflections northward (2), indicating the presence of fluids in the sediments below Penta Palummo
 1376 area. Upward the Unit C, is characterized by parallel reflectors (3) from North to South. The change
 1377 of the seismic facies from (2) to (3) indicate that Unit B corresponds to an impermeable seal. (c)
 1378 Single channel seismic reflection profile showing evidence for the migration of fluids, that are present
 1379 in the Unit C, until the seafloor in the area where the pyroclastic units are absent.

1380

1381 **Figure 6.** (a) Relocated seismicity 2014–2023 — its surface distribution and vertical projections
 1382 along the XY axes — in the Campi Flegrei area (redrawn from Tan et al., 2025), also shown the traces
 1383 of the syncline and anticline axes of Fig. 2a. The reference point is Rite Station (14.14°E, 40.82°N).
 1384 (b) Strain distribution within a fold showing extension in correspondence of the anticline (X) and of
 1385 the syncline (Y) respectively above and below the neutral surface (from Ramsay, 1967). (c) Structural
 1386 and stratigraphic compartmentalization showing as the permeability is strictly controlled by the
 1387 fractures and strata permeability. The comparison with the Pozzuoli Anticline and the depth of
 1388 earthquakes suggests a neutral surface at 2/2.5 km of depth.

1389

1390 **Figure 7.** (a) Daily rainfall measurements across Campi Flegrei since 1970. (b) Rainwater 1-year
 1391 cumulative curve (blue line), with its multi-year smooth curve (red line); (c) Ground displacement
 1392 (blue line) at the GNSS Rite Station with its multi-year smooth curve (red line). (d) Residual vertical
 1393 displacement obtained by detrending the red curve from the blue curve in (c), which highlights several
 1394 mini uplifts. The high rainfall events indicated by the points A, B, C and D in panel (b) are interpreted
 1395 to have driven the significant mini-uplifts shown in panel (d) with time lags of about 4 years before
 1396 2005 and about 3 years after 2010.

1397

1398 **Figure 8.** Comparison between modelled groundwater accumulation and vertical ground movement
 1399 as a function of the discharge time scale $\tau(t)$. (a₁) and (a₂) show the output of Eq. (13) in the model
 1400 under the two conditions: (1) constant $\tau(t)$; (2) variable $\tau(t)$. (b₁) and (b₂), which are equal for
 1401 comparison, show the ground displacement at the GNSS Rite Station; note the close multidecadal
 1402 correlation between (a₂) and (b₂). (c₁) and (c₂) show the curves in (a₁) and (a₂) detrended of their
 1403 interannual component after removing the smooth components. (d₁) and (d₂), which are equal for
 1404 comparison, show the curves in (b₁) and (b₂) detrended of their interannual component after removing
 1405 the smooth components.

1406

1407 **Declaration of interests**

1408 The authors declare that they have no known competing financial interests or personal
 1409 relationships that could have appeared to influence the work reported in this paper.

1411 Co-author Nicola Scafetta is an Editor of this journal and was not involved in the editorial
 1412 review or the decision to publish this article.

1413

1414 The authors declare the following financial interests/personal relationships which may be
1415 considered as potential competing interests:
1416

1417
1418
1419
1420
1421

1422

1423 **Highlights:**

1424

1425 Pozzuoli downtown uplifted by 1.4 meters between 2005 and January 2025.
1426 Uplift and associated seismicity are partially induced by rainwater infiltration.
1427 Two separated water reservoirs above and below about 2 km are identified.
1428 Rainwater accumulation below Pozzuoli accounts for over 20% of total ground uplift.
1429 It is proposed surface drainage to reduce ground uplift and seismicity.
1430